7-15-2013

Synthetic, Spectroscopic and DFT Studies of Iron Complexes with Iminobenzo(semi)quinone Ligands: Implications for o-Aminophenol Dioxygenases

Michael M. Bittner
Marquette University, michael.bittner@marquette.edu

David S. Krause
Ursinus College

Sergey V. Lindeman
Marquette University, sergey.lindeman@marquette.edu

Cordina V. Popescu
Ursinus College

Adam T. Fiedler
Marquette University, adam.fiedler@marquette.edu

Accepted version. *Chemistry - A European Journal*, Vol. 19, No. 29 (July 2013): 9686-9698. DOI.

Synthetic, Spectroscopic and DFT Studies of Iron Complexes with Iminobenzo(semi)quinone Ligands: Implications for o-Aminophenol Dioxygenases

Michael M. Bittner
Department of Chemistry, Marquette University
Milwaukee, WI

David Kraus
Department of Chemistry, Ursinus College
Collegeville, PA

Dr. Sergey V. Lindeman
Department of Chemistry, Marquette University
Milwaukee, WI

Dr. Codrina V. Popescu
Department of Chemistry, Ursinus College
Collegeville, PA

Dr. Adam T. Fiedler
Department of Chemistry, Marquette University
Milwaukee, WI

Chemistry, a European Journal, Vol. 19, No. 29 (July 2013): pg. 9686-9698. DOI.

Abstract:

The oxidative C-C bond cleavage of *o*-aminophenols by nonheme Fe dioxygenases is a critical step in both human metabolism (the kynurenine pathway) and the microbial degradation of nitroaromatic pollutants. The catalytic cycle of *o*-aminophenol dioxygenases (APDOs) has been proposed to involve formation of an Fe(II)/O_2/iminobenzosemiquinone complex, although the presence of a substrate radical has been called into question by studies of related ring-cleaving dioxygenases. Recently, we reported the first synthesis of an iron(II) complex coordinated to an iminobenzosemiquinone (ISQ) ligand, namely, [Fe(^{Ph2}Tp)(ISQ^{tBu})] (**2a**; where ^{Ph2}Tp = hydrotris(3,5-diphenylpyrazol-1-yl)borate and ISQ^{tBu} is the radical anion derived from 2-amino-4,6-di-*tert*-butylphenol). In the current manuscript, density functional theory (DFT) calculations and a wide variety of spectroscopic methods (electronic absorption, Mössbauer, magnetic circular dichroism, and resonance Raman) were employed to obtain detailed electronic-structure descriptions of **2a** and its one-electron oxidized derivative [**3a**]$^+$. In addition, we describe the synthesis and characterization of a parallel series of complexes featuring the neutral supporting ligand tris(4,5-diphenyl-1-methylimidazol-2-yl)phosphine (^{Ph2}TIP). The isomer shifts of ~0.97 mm/s obtained via Mössbauer experiments confirm that **2a** (and its ^{Ph2}TIP-based analogue [**2b**]$^+$) contain Fe(II) centers, and the presence of an ISQ radical was verified by analysis of the absorption spectra in light of time-dependent DFT calculations. The collective spectroscopic data indicate that one-electron oxidation of the Fe^{2+}–ISQ complexes yields complexes ([**3a**]$^+$ and [**3b**]$^{2+}$) with electronic configurations between the Fe^{3+}–ISQ and Fe^{2+}–IBQ limits (IBQ = iminobenzoquinone), highlighting the ability of *o*-amidophenolates to access multiple oxidation states. The implications of these results for the mechanism of APDOs and other ring-cleaving dioxygenases are discussed.

Introduction

A critical step in the microbial degradation of numerous aromatic compounds involves oxidative ring scission by a mononuclear nonheme Fe dioxygenase.[1] Ring-cleaving dioxygenases have been shown to oxidize an impressive array of substrates, including catechols, protocatechuates,[2] *o*-aminophenols,[3] hydroquinones,[4] and salicylates.[5] The general catalytic strategy employed by these dioxygenases differs substantially from the "textbook" O_2-activation mechanism exemplified by the cytochrome P450s,[6] methane monooxygenase,[7] and α-ketoglutarate-dependent dioxygenases.[8] In this latter set of enzymes, O_2 is used to generate an iron(IV)-oxo

Chemistry, a European Journal, Vol. 19, No. 29 (July 2013): pg. 9686-9698. DOI.

(ferryl) intermediate that performs the demanding hydroxylation of an aliphatic substrate. By contrast, extensive experimental and computational studies have revealed that the ring-cleaving dioxygenase mechanism does not involve high-valent Fe intermediates, as illustrated for the extradiol catechol dioxygenases (ECDOs) and *o*-aminophenol dioxygenases (APDOs) in Scheme 1.[2c, 9] In both cases, the bidentate substrate coordinates to the Fe(II) center as a monoanionic ligand. Displacement of the bound H_2O molecules facilitates formation of an Fe/O_2 adduct capable of reacting directly with the bound substrate. The resulting peroxy-bridged intermediate undergoes a Criegee rearrangement to generate a lactone, which is hydrolyzed by the Fe-OH unit to provide the ring-opened product. Several of these intermediates were observed crystallographically in different subunits of the enzyme homoprotocatechuate 2,3-dioxygenase (HPCD).[10]

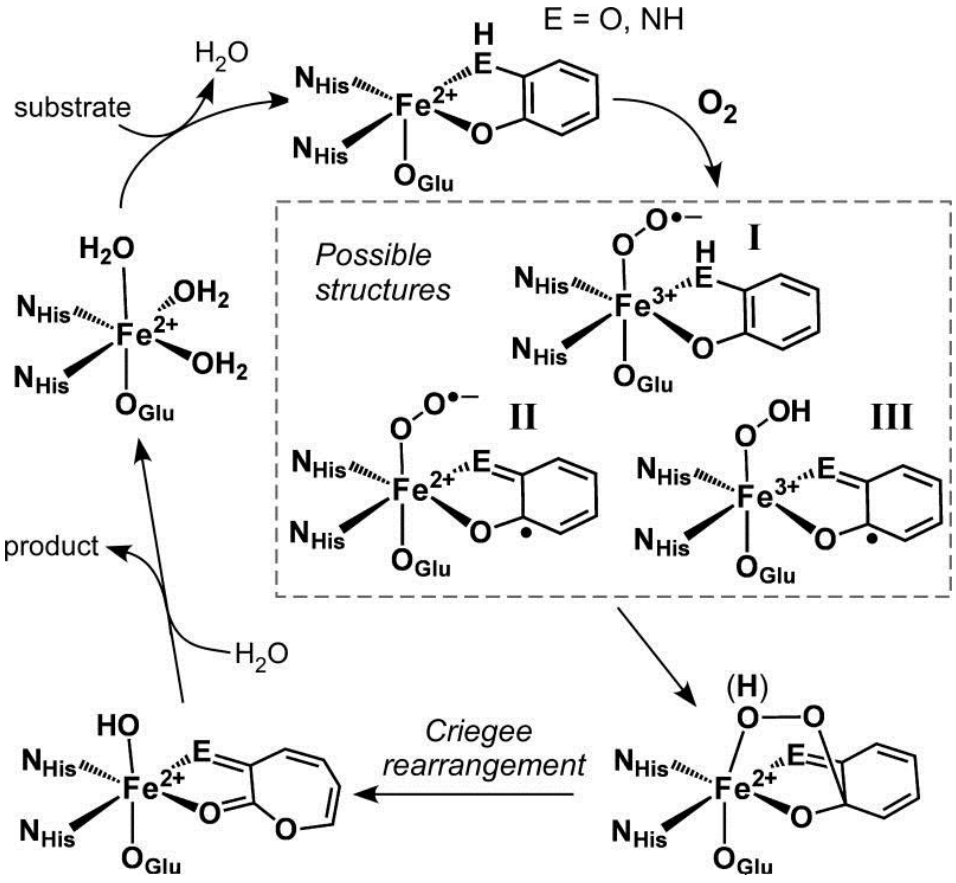

Scheme 1

Chemistry, a European Journal, Vol. 19, No. 29 (July 2013): pg. 9686-9698. DOI.

While there is broad agreement concerning the generic mechanism shown in Scheme 1, the electronic structure of the critical Fe/O_2/substrate intermediate remains disputed. While Fe/O_2 adducts are normally described as ferric-superoxo species (such as intermediate **I** in Scheme 1), early studies by Lipscomb[11] and Bugg[12] lead to the proposal that ring-cleaving dioxygenases proceed instead via a superoxo-Fe(II)-(imino)semiquinone species (**II**). The radical character of the substrate was presumed to facilitate reaction with the superoxo ligand, thereby overcoming the large kinetic barrier to formation of the peroxy intermediate. This hypothesis was partly inspired by model studies that had demonstrated the "non-innocent" nature of metal-bound catecholates[13] and amidophenolates.[14] [15] [16] [17] [18] [19] Subsequent experiments with a substrate analogue featuring a cyclopropyl moiety as a radical probe indicated formation of a semiquinonate (SQ) radical during the catalytic cycle of MhpC, a well-studied ECDO.[20] Density functional theory (DFT) analysis by Siegbahn further supported this electronic structure description.[21] In addition, Emerson *et al.* demonstrated that a pair of ECDOs, Fe-HPCD and Mn-MndD, are equally active with either Fe or Mn in their active sites, despite the intrinsically different redox potential of the two metal ions.[22] This result lead to the conclusion that the Fe (or Mn) oxidation state does not change during the catalytic cycle; instead, the metal ion only serves to conduct an electron from the bound substrate ligand to O_2, thus yielding intermediate **II** directly.

Despite this large body of evidence, recent studies have challenged the prevailing notion that a substrate-based radical is generated in the catalytic cycles of ECDOs (and, by extension, other ring-cleaving dioxygenases). Firstly, Lipscomb and coworkers succeeded in isolating the Fe/O_2 adduct of a HPCD mutant (H200N) bound to the "unactivated" substrate 4-nitrocatechol. Interrogation with EPR and Mössbauer spectroscopies revealed that this species contains an Fe^{3+}–$O_2^{\bullet-}$ unit with $S = 2$ – inconsistent with the presence of a SQ ligand.[23] A follow-up study of H200N HPCD with the native substrate resulted in the isolation and spectroscopic characterization of novel intermediate best described as a hydroperoxo-Fe(III)-semiquinone species (**III** in Scheme 1).[24] However, a recent computational study by Ye and Neese suggested that this intermediate is not catalytically viable.[25] Their calculations of the ECDO mechanism found no evidence that a SQ-containing intermediate (either **II** or **III**)

Chemistry, a European Journal, Vol. 19, No. 29 (July 2013): pg. 9686-9698. DOI.

is required for catalysis. Instead, they favor a mechanism in which the ferric-superoxo adduct (**I**) converts directly to a hydroperoxo-bridged species (Scheme 1). The kinetic barrier for this step is lowered by concomitant transfer of a proton from the second-sphere histidine residue to the nascent peroxo group.

The development of suitable synthetic models can help resolve the ambiguous electronic structures of enzymatic intermediates. In a recent communication, we described the synthesis and X-ray structure of the five-coordinate (5C) complex **2a** (Scheme 2) that represents the first synthetic example of an Fe(II) center coordinated a biologically-relevant (imino)semiquinonate ligand.[26] The supporting ligand in **2a** is hydrotris(3,5-diphenylpyrazol-1-yl)borate (^{Ph2}Tp), which adequately models the facial coordination geometry and monoanionic charge of the 2-His-1-carboxylate coordination motif of most ring-cleaving dioxygenases.[27] A combination of crystallographic, spectroscopic (absorption, EPR), and computational methods were used to confirm the existence of the ^{tBu}ISQ ligand in **2a**. The overall spin of 3/2 arises from antiferromagnetic (AF) coupling between the high-spin Fe(III) center (S = 5/2) and ISQ radical. Using similar techniques, we also examined the complex [**3a**]SbF_6 that arises from one-electron oxidation of **2a**. The X-ray structural data for [**3a**]$^+$ are consistent with the presence of an Fe^{3+}–^{tBu}ISQ unit with S = 2, although density functional theory (DFT) calculations suggested a certain degree of Fe^{2+}–^{tBu}IBQ character (where ^{tBu}IBQ is the neutral iminobenzoquinone with *tert*-butyl substituents at the 4- and 6-positions).[26]

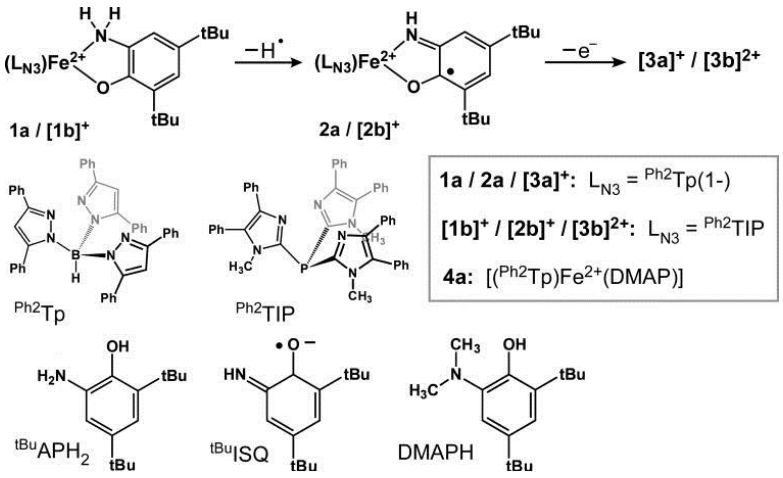

Scheme 2

Chemistry, a European Journal, Vol. 19, No. 29 (July 2013): pg. 9686-9698. DOI.

In this manuscript, we seek to develop detailed electronic-structure descriptions of **2a** and [**3a**]$^{+}$ using an assortment of spectroscopic methods, including UV-vis-NIR absorption, Mössbauer, magnetic circular dichroism (MCD), and resonance Raman (rR) spectroscopies. In addition, we have prepared a parallel series of complexes (**1b, 2b**, and [**3b**]$^{+}$) containing the facial N_3-donor ligand tris(4,5-diphenyl-1-methylimidazol-2-yl)phosphine[28] (^{Ph2}TIP; Scheme 2). X-ray structures of complexes [**1b**]BPh_4 and [**3b**]$(OTf)_2$ are presented to complement those already published for **1a, 2a**, and [**3a**]SbF_6. By employing this neutral supporting ligand, we are able to evaluate the role of coordination environment in modulating the oxidation states of the Fe center and ISQ ligand. In all cases, the spectroscopic data were analyzed with the aid of DFT calculations. By elucidating the spectroscopic signatures of these synthetic complexes, we anticipate that our results will assist in the interpretation of comparable data from the biological systems, thereby allowing researchers to determine whether Fe–(I)SQ species are viable intermediates in the catalytic cycles of ring-cleaving dioxygenases.

Results and Analysis

1. Preparation, Structural Characterization, and Electrochemical Properties

1.A. Fe(II) Complexes The synthesis and X-ray structure of [Fe^{2+}(^{Ph2}Tp)(^{tBu}APH)] (**1a**) were reported in our previous paper.[26] The analogous complex [**1b**]$^{+}$ based on the neutral ^{Ph2}TIP ligand was generated by mixing [Fe^{2+}(^{Ph2}TIP)$(OTf)_2$][28] and 2-amino-4,6-di-*tert*-butylphenol ($^{tBu}APH_2$) with one equivalent of triethylamine in CH_2Cl_2; recrystallization from toluene/pentane provided [**1b**]OTf as a yellow solid. Following counteranion metathesis with $NaBPh_4$, X-ray quality crystals of [**1b**]BPh_4 were obtained by layering a concentrated 1,2-dichloroethane (DCE) solution with MeOH. The resulting structure (Figure 1) contains two symmetrically independent [**1b**]$^{+}$ units with nearly identical geometries. Relevant structural parameters for **1a**, [**1b**]BPh_4, and **4a** are provided in Table 1. Similar to **1a**, complex [**1b**]$^{+}$ features a 5C monoiron(II) center in a distorted trigonal-bipyramidal coordination environment (τ = 0.60[29]). The amino and phenolate donors of the bidentate ^{tBu}APH ligand are found in axial and

Chemistry, a European Journal, Vol. 19, No. 29 (July 2013): pg. 9686-9698. DOI.

equatorial positions, respectively (Figure 1). The average Fe-N_{TIP} bond distance of 2.19 Å in [**1b**]$^{+}$ is ~0.04 Å longer than the average Fe-N_{Tp} distance in **1a**, reflecting the weaker donating ability of neutral ^{Ph2}TIP relative to anionic ^{Ph2}Tp. In both **1a** and [**1b**]$^{+}$, the Fe-N/O bond lengths are indicative of high-spin Fe(II) centers, consistent with the presence of paramagnetically-shifted peaks in the corresponding ^{1}H NMR spectra (Figure S1).

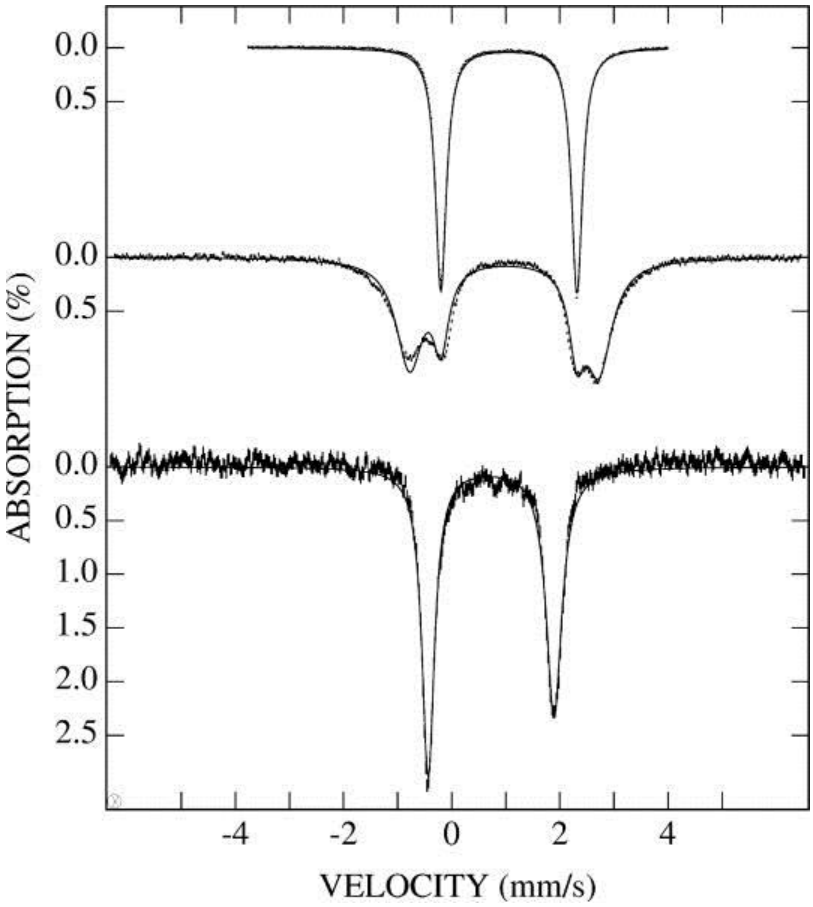

Figure 1 Thermal ellipsoid plots (50% probability) derived from the X-ray structures of [**1b**]BPh_4•1.5DCE (top) and **4a**•$4CH_2Cl_2$ (bottom). Non-coordinating solvent molecules, counteranions, and most hydrogen atoms have been omitted for clarity. Key metric parameters are provided in Table 1.

Chemistry, a European Journal, Vol. 19, No. 29 (July 2013): pg. 9686-9698. DOI.

	1a•MeCN•0.5DCE	1b[BPh_4] • 1.5DCE	4a•4CH_2Cl_2
Fe1-N1	2.101(1)	2.175(2)	2.121(2)
Fe1-N3	2.127(1)	2.175(2)	2.158(2)
Fe1-N5	2.223(1)	2.222(2)	2.236(2)
Fe1-O1	1.931(1)	1.929(2)	1.920(2)
Fe1-N7	2.214(1)	2.229(2)	2.335(2)
N1-Fe1-N3	92.82(5)	92.50(7)	100.11(9)
N1-Fe1-N5	83.30(5)	85.88(7)	80.90(9)
N3-Fe1-N5	86.11(5)	84.43(6)	81.79(9)
O1-Fe1-N1	136.61(5)	134.21(7)	131.71(9)
O1-Fe1-N3	129.47(5)	130.73(7)	127.63(9)
O1-Fe1-N5	105.94(4)	109.45(6)	109.69(9)
O1-Fe1-N7	80.76(4)	80.24(6)	78.07(8)
N1 -Fe-N7	92.60(5)	88.33(7)	100.11(9)
N3 -Fe-N7	88.68(5)	87.90(7)	98.07(9)
N5 -Fe-N7	173.20(5)	170.17(7)	170.40(9)
τ-value[a]	0.61	0.60	0.65

Table 1 Selected Bond Distances (Å) and Bond Angles (deg) from the X-ray Structures of **1a**•MeCN•0.5DCE, **1b**[BPh_4] • 1.5DCE, and **4a**•4CH_2Cl_2.

The ^{Ph2}Tp-based complex **4a** contains the DMAP(1-) ligand – the *N,N*-dimethylated version of ^{tBu}APH (Scheme 2). This complex is intended serve as a "control", since methylation of the – NH_2 group hinders conversion to the ISQ state. The overall structure of **4a**, as revealed by X-ray crystallography (Figure 1), is quite similar to **1a**. The most prominent difference is the 0.12 Å elongation of the Fe1-N7 bond in **4a** relative to **1a** (Table 1), presumably due to steric repulsion between the $-NMe_2$ group and 3-Ph substituents of the ^{Ph2}Tp ligand. Additionally, the plane of the DMAPH ligand is bent away from the O1-Fe-N7 chelate ring by 26°, whereas the two planes are nearly colinear in **1a** and [**1b**]$^+$.

1.B. Fe(II)-Iminobenzosemiquinonate Complexes Previously, we demonstrated that reaction of **1a** with 2,4,6-tri-*tert*-butylphenoxy radical (TTBP$^•$) provides the complex [Fe(^{Ph2}Tp)(^{tBu}ISQ)] (**2a**) via H-

Chemistry, a European Journal, Vol. 19, No. 29 (July 2013): pg. 9686-9698. DOI.

atom transfer from the ^{tBu}APH $-NH_2$ donor to the organic radical.[26] In the X-ray structure of **2a**, the ^{tBu}ISQ ligand exhibits short O-C and N-C bond distances and a "four long/two short" distortion of the C-C bonds (Table S1) – well-known traits of the iminobenzosemiquinone oxidation state as elucidated by Wieghardt[15-17], Kaim,[14] and others.[19] Further spectroscopic evidence in support of this electronic-structure description is provided later in the manuscript.

Treatment of [**1b**]OTf with TTBP$^{\bullet}$ in CH_2Cl_2 produces a light green chromophore [**2b**]$^+$ with an absorption spectrum similar to the one collected for **2a** (Figure 2). In addition, the EPR spectra of [**2b**]$^+$ and **2a** are nearly identical; both exhibit a sharp peak at $g \sim 6.5$ and a broad derivative feature centered at $g < 1.8$ (Figure S2). Such spectra are characteristic of $S = 3/2$ systems with large, negative D-values and moderate rhombicities ($E/D = 0.24$ and 0.18 for **2a** and [**2b**]$^+$, respectively). Unfortunately, despite repeated attempts, it was not possible to obtain X-ray quality crystals of [**2b**]$^+$. However, the strong resemblance between the spectroscopic (UV-vis/EPR) features of **2a** and [**2b**]$^+$ suggests similar Fe^{2+}–ISQ electronic configurations – an assumption verified by analysis with Mössbauer spectroscopy (*vide infra*).

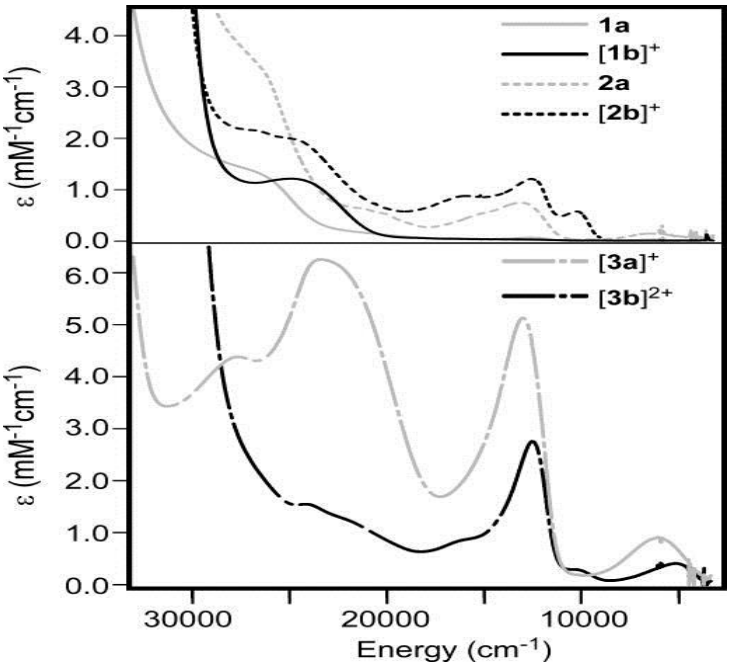

Figure 2 UV-vis-NIR absorption spectra obtained in CH_2Cl_2 at room temperature.

Chemistry, a European Journal, Vol. 19, No. 29 (July 2013): pg. 9686-9698. DOI.

1.C. Complexes [3a]SbF_6 and [3b]$(OTf)_2$ Oxidation of **1a** and [**1b**]OTf with two equivalents of AgX (X = SbF_6 or OTf) in CH_2Cl_2 gives rise to complexes [**3a**]SbF_6 and [**3b**]$(OTf)_2$, respectively, that each display a distinctive absorption band near 780 nm (12,800 cm^{-1}; Figure 2). The magnetic moments of these complexes are near 5.0 μ_B – typical for S = 2 paramagnets – and the EPR spectrum of $[\mathbf{3b}]^{2+}$ exhibits a 4S signal at g = 8.7 (Figure S3). The structural data for [**3a**]SbF_6 reported in our earlier study suffers from large uncertainties in bond distances (3σ ~ 0.035 Å in C-C distances), which hindered evaluation of the ligand oxidation state based on geometric parameters. As noted in the introduction, DFT calculations suggested an electronic structure intermediate between Fe^{3+}–^{tBu}ISQ and Fe^{2+}–^{tBu}IBQ.[26]

Crystals of [**3b**]$(OTf)_2$ were obtained by layering a CH_2Cl_2 solution with pentane; the resulting X-ray structure is shown in Figure 3, and relevant metric parameters for [**3a**]SbF_6 and [**3b**]$(OTf)_2$ are compared in Table 2. The σ-values for the [**3b**]$(OTf)_2$ bond distances are significantly smaller than those in the [**3a**]SbF_6 structure. Like $[\mathbf{3a}]^+$, complex $[\mathbf{3b}]^{2+}$ features a distorted trigonal-bipyramidal coordination geometry (τ = 0.57) with O1 occupying an axial position. The O1-C1, N7-C2, and C-C bond distances of the *O,N*-donor ligand are fully consistent with ligand-based oxidation. Recently, Brown developed a helpful procedure for assessing the oxidation state of *o*-amidophenolate ligands based on their metric parameters.[30] Using this method, the ligands in $[\mathbf{3a}]^+$ and $[\mathbf{3b}]^{2+}$ have estimated charges of −0.54(8) and −0.48(10) – approximately half-way between the ISQ^{1-} and IBQ^0 limits (Table 3). Further insights into the Fe and ligand oxidation state of $[\mathbf{3a}]^+$ and $[\mathbf{3b}]^{2+}$ are provided by spectroscopic and computational studies described below.

Chemistry, a European Journal, Vol. 19, No. 29 (July 2013): pg. 9686-9698. DOI.

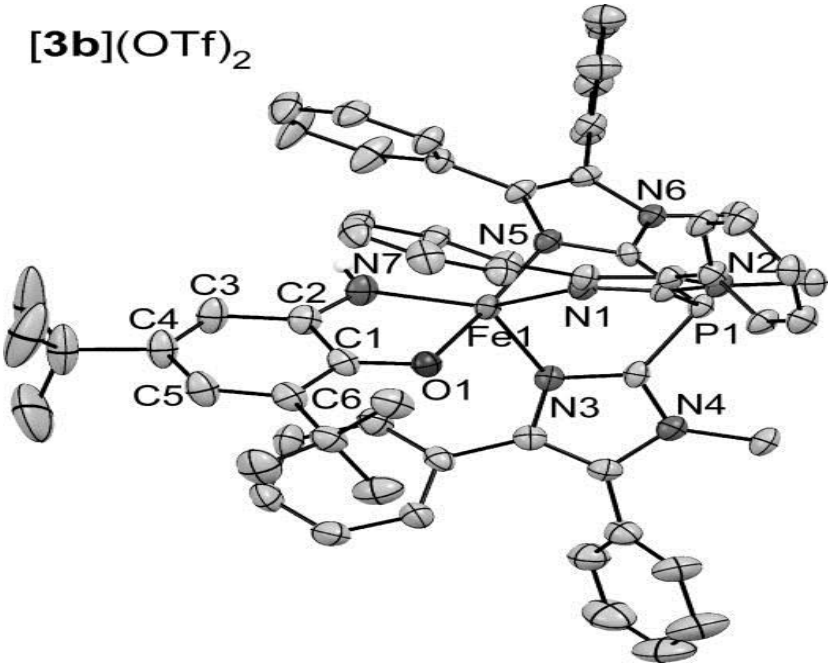

Figure 3 Thermal ellipsoid plot (50% probability) derived from the X-ray structure of [**3b**](OTf)$_2$•CH_2Cl_2. Non-coordinating solvent molecules, counteranions, and most hydrogen atoms have been omitted for clarity. Key metric parameters are provided in Table 2.

	[3a]SbF_6	[3b](OTf)$_2$
Fe1-N1	2.071(7)	2.077(3)
Fe1-N3	2.038(7)	2.089(4)
Fe1-N5	2.134(6)	2.093(4)
Fe1-O1	2.082(6)	2.037(3)
Fe1-N7	2.017(8)	2.013(4)
O1-C1	1.264(11)	1.287(5)
N7-C2	1.333(11)	1.314(6)
C1-C2	1.473(12)	1.483(6)
C2-C3	1.423(12)	1.429(6)
C3-C4	1.345(15)	1.340(7)
C4-C5	1.433(16)	1.448(7)
C5-C6	1.375(14)	1.370(7)
C1-C6	1.439(12)	1.427(7)

Table 2 Selected Bond Distances (Å) from the X-ray Structures of [3a]SbF_6•0.5DCE and [3b](OTf)$_2$•1.5CH_2Cl_2.

Chemistry, a European Journal, Vol. 19, No. 29 (July 2013): pg. 9686-9698. DOI.

			1a	$[1b]^+$	2a	$[2b]^+$	$[3a]^{+,a}$	$[3b]^{2+,a}$
Metric parameters	Fe-$N_{Tp/TIP}$ ave (Å)	exp	2.150	2.191	2.137	*2.233*	2.081	2.086
		DFT	*2.215*	*2.240*	*2.188*		*2.077*	*2.122*
	O1-C1 (Å)	exp	1.345	1.340	1.285	*1.277*	1.264	1.287
		DFT	*1.330*	*1.338*	*1.276*		*1.278*	*1.273*
	N7-C2 (Å)		1.451	1.455	1.328	*1.337*	1.333	1.314
			1.454	*1.460*	*1.335*		*1.329*	*1.326*
	Ligand charge	exp	—	—	–0.69	*–0.73*	–0.54	–0.48
		DFT			*–0.72*		*–0.62*	*–0.54*
Mulliken spins	Fe	*DFT*	*+3.78*	*+3.76*	*+3.77*	*+3.76*	*+3.94*	*+3.93*
	O,N-ligand	*DFT*	*+0.14*	*+0.18*	*–0.86*	*–0.82*	*–0.30*	*–0.15*
Mössbauer	δ (mm/s)	exp	1.06	1.06 / 1.14	0.97	0.95 / 0.99	0.73	0.64
		DFT	*0.96*	*0.95*	*0.86*	*0.91*	*0.57*	*0.62*
	ΔE_Q (mm/s)	exp	2.52	2.08/2.93	3.5	1.9[b] / 2.5	2.33	1.94
		DFT	*2.00*	*1.86*	*2.93*	*2.09*	*0.71*	*1.34*

Table 3 Experimental and DFT-Computed Properties of Selected Complexes.

1.D. Electrochemical Properties Our original intent in performing chemical oxidations of **1a** and [**1b**]OTf was to generate the corresponding ferric complexes $[Fe^{3+}(^{Ph2}Tp)(^{tBu}APH)]^+$ ([**1a^{ox}**]$^+$) and $[Fe^{3+}(^{Ph2}TIP)(^{tBu}APH)]^{2+}$ ([**1b^{ox}**]$^{2+}$). However, treatment of **1a** and [**1b**]OTf with a single equivalent of one-electron oxidants (such as acetylferrocenium, $[N(C_6H_4Br\text{-}4)_3]^+$, or Ag^+) instead produced 0.5 equivalent of [**3a**]$^+$ and [**3b**]$^{2+}$, respectively. Indeed, titrations of **1a** and [**1b**]OTf with acetylferrocenium revealed a linear increase in the intensity of the [**3a**]$^+$/[**3b**]$^{2+}$ absorption features up to two equivalents of oxidant, indicating that the Fe(II) precursors exclusively undergo two-electron oxidations. This situation generally occurs when the product of the initial one-electron transfer undergoes a chemical change to yield a species that is more reducing than the starting complex.

To better understand this phenomenon, cyclic voltammetric studies of the ^{Ph2}Tp series were conducted in CH_2Cl_2 with 100 mM $[NBu_4]PF_6$ as the supporting electrolyte.[31] All redox potentials are referenced to the ferrocenium/ferrocene couple (Fc^+/Fc). As shown in Figure 4, **1a** undergoes an irreversible oxidation at −15 mV, followed

Chemistry, a European Journal, Vol. 19, No. 29 (July 2013): pg. 9686-9698. DOI.

by a cathodic wave at −490 mV with half the current intensity of the anodic wave. We therefore concluded that the oxidation at −15 mV corresponds to the two-electron process **1a** → [**3a**]$^+$ + H$^+$, while the subsequent reduction corresponds to one-electron reduction of [**3a**]$^+$ to **2a**. This conclusion was confirmed by the CV of **2a** (Figure 4), which shows a quasi-reversible [**3a**]$^+$/**2a** couple with $E_{1/2}$ = −380 mV (ΔE = 140 mV). Thus, **2a** is indeed more reducing than **1a**, accounting for the behavior described above.

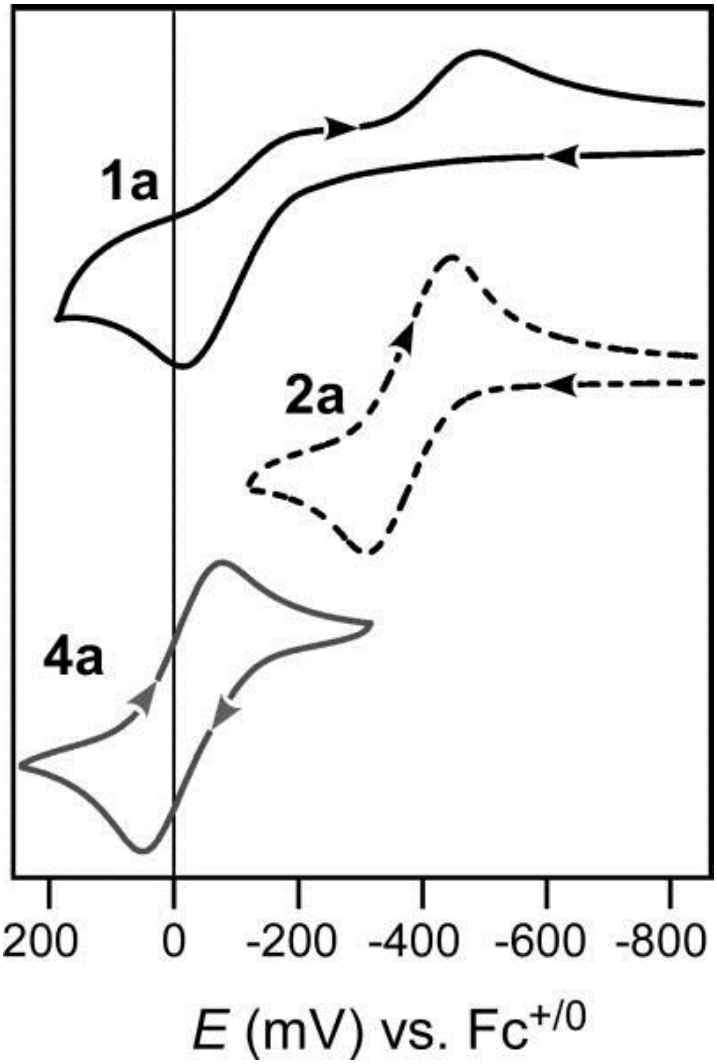

Figure 4 Cyclic voltammograms of **1a, 2a**, and **4a**. Data was collected in CH_2Cl_2 with 100 mM $(NBu_4)PF_6$ as the supporting electrolyte. The scan rate was either 100 mV/s (**2a** and **4a**) or 200 mV (**1a**).

Chemistry, a European Journal, Vol. 19, No. 29 (July 2013): pg. 9686-9698. DOI.

Scheme 3 summarizes the electrochemical properties of these complexes. One-electron oxidation of **1a** presumably yields the ferric complex [**1a^{ox}**]$^+$, although this transient species is never observed. Instead, [**1a^{ox}**]$^+$ quickly sheds a proton to the surrounding medium to give **2a**, since the change in Fe oxidation state dramatically lowers the pK_a of the coordinated –NH_2 donor. The fact that $E_{p,a}$([**1a^{ox}**]$^+$/**1a**) > $E_{1/2}$([**3a**]$^+$/**2a**) ensures that **2a** is not stable in this environment; instead, it disproportionates to give 0.5 equivalent each of **1a** and [**3a**]$^+$ (Scheme 3B). Thus, the only way to convert **1a** into **2a** is to employ an H-atom abstracting agent like TTBP$^\bullet$ that is not an effective one-electron oxidant. Our results also indicate that deprotonation of the *O,N*-ligand dramatically lowers its redox potential, thus favoring ligand-based over metal-based oxidation.

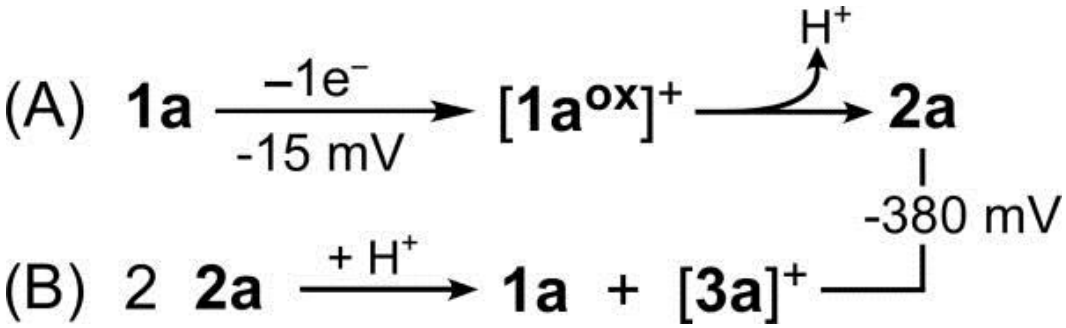

Scheme 3

The electrochemical behavior of **4a** is straightforward since the DMAPH ligand cannot easily participate in proton or electron transfers. This complex displays a quasi-reversible redox event with $E_{1/2}$ = −15 mV (ΔE = 130 mV) that corresponds to the Fe^{3+}/Fe^{2+} couple (Figure 4). The **4a** potential can serve as an approximate value for the irreversible [**1a^{ox}**]$^+$/**1a** couple. The free $^{tBu}APH_2$ and DMAPH ligands are irreversibly oxidized at more positive potentials of +280 and +450 mV, respectively, in CH_2Cl_2 (Figure S4).

Chemistry, a European Journal, Vol. 19, No. 29 (July 2013): pg. 9686-9698. DOI.

2. Spectroscopic and Computational Analysis of Electronic Structures

2.A. Geometric and Electronic Structures of DFT-Optimized Models

Since the spectroscopic data presented below are frequently interpreted with the assistance of DFT calculations, it is necessary to first describe the molecular and electronic structures of our computational models. We employed truncated versions of the complexes in which the *tert*-butyl groups of the *O,N*-donor were replaced with methyl groups and the phenyl substituents at the 5-positions of the pyrazole (^{Ph2}Tp) and imidazole (^{Ph2}TIP) rings were removed. Unless otherwise noted, all calculations employed the B3LYP functional. As noted in our earlier study, the most stable geometry-optimized structure of **2a** was obtained using the broken symmetry (BS) methodology[32] and an overall spin of 3/2; this model provided metric parameters in excellent agreement with the crystallographic data (Table S1). The Mulliken spin populations, listed in Table 3, support the view that the electronic structure of **2a** should be described as a high-spin Fe(II) center (3.77 α-spins) AF-coupled to an ISQ-based π-radical (0.86 β-spins). The exchange coupling constant (J) has a computed value of −223 cm^{-1}, based on the Yamaguchi approach ($H = -2JS_A \bullet S_B$).[33] The AF coupling is mediated by a nonorthogonal pair of singly-occupied molecular orbitals (SOMOs) with opposite spins, shown in the qualitative MO diagram in Figure 5. The relevant magnetic orbitals for **2a** are the α-Fe(d_{xy})- and β-ISQ(π*)-based MOs that display 33% spatial overlap – indicative of a ligand-based radical with rather weak interactions with the Fe(II) center. The structure and bonding scheme of [**2b**]$^+$, also computed with the BS approach, are nearly identical to the corresponding **2a** model (Tables 3 and S1), consistent with the spectral similarities between **2a** and [**2b**]$^+$ (*vide supra*).

Chemistry, a European Journal, Vol. 19, No. 29 (July 2013): pg. 9686-9698. DOI.

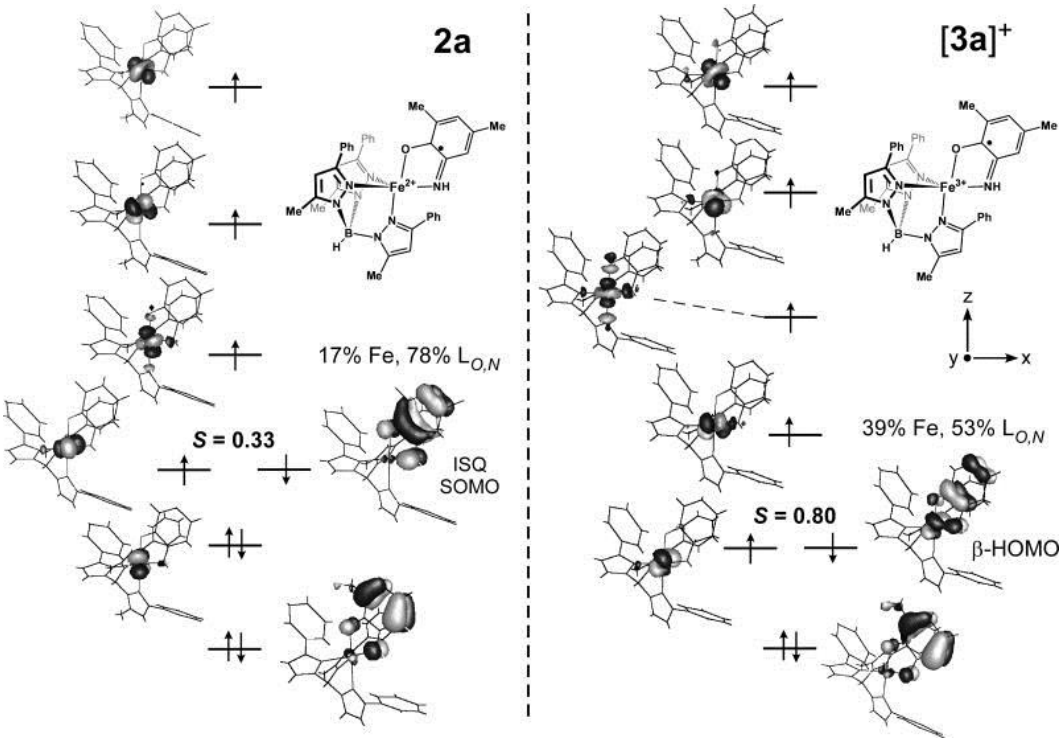

Figure 5 Qualitative molecular orbital diagrams of **2a** (left) and [**3a**]$^+$ (right) obtained from broken-symmetry DFT calculations. Isosurface plots for important MOs are provided, along with the overlap (*S*) between corresponding magnetic orbitals.

While the optimized [**3a**]$^+$ geometry obtained with the B3LYP functional agrees reasonably well with the crystallographic data, the Fe-N/O and intraligand bond distances in the DFT-structure of [**3b**]$^{2+}$ structure deviate significantly from the experimental values (Table S2). Better agreement was obtained with the BP functional for both [**3a**]$^+$ and [**3b**]$^{2+}$, and therefore our analysis of these complexes has employed the BP-derived structures. For each complex, DFT calculations converge to the same S = 2 state irrespective of whether the BS approach is employed. The Mulliken spin populations appear to favor an Fe^{2+}–^{tBu}IBQ description, as the Fe center carries approximately four unpaired spins and the ligand-based spin density is reduced relative to **2a**/[**2b**]$^+$ (Table 3). The β-HOMO of [**3a**]$^+$ contains significant amounts of both Fe (39%) and *O,N*-ligand (53%) character (Figure 5), indicative of intermediate Fe$^{2+/3+}$ and IBQ/ISQ oxidation states (the corresponding values for [**3b**]$^{2+}$ are 53 and 37%). In addition, the spatial overlap between the pair of magnetic orbitals involved in the spin-coupling interaction is ~80%, which reflects a high

Chemistry, a European Journal, Vol. 19, No. 29 (July 2013): pg. 9686-9698. DOI.

degree of spin pairing (as opposed to the "diradical" situation of **2a**). However, these computational results should be viewed with caution, since the experimental metric parameters for [**3a**]$^{+}$/[**3b**]$^{2+}$ are not consistent with a pure IBQ description, as evident in the ligand charges shown in Table 3. Spectroscopic studies are therefore required to properly evaluate the electronic structures of [**3a**]$^{+}$ and [**3b**]$^{2+}$.

Finally, we generated DFT models of the hypothetical Ga(III) complexes, [Ga^{3+}(^{Ph2}Tp)(ISQ)]$^{+}$ (**Ga-ISQ**) and [Ga^{3+}(^{Ph2}Tp)(IBQ)]$^{2+}$ (**Ga-IBQ**). The Ga(III) ion has been employed in previous computational studies as a closed-shell analog of Fe(III) due to similarities in charge and ionic radius.[34] Since Ga(III) is not redox active, the **Ga-ISQ** and **Ga-IBQ** models allow us to assess the electronic and spectroscopic properties of "pure" ISQ and IBQ ligands without complications from the paramagnetic Fe center.

2.B. Mössbauer Spectroscopy

Mössbauer (MB) spectroscopy has proven capable of providing definitive assessments of Fe oxidation states in complexes with non-innocent ligands. Figure 6 displays low-temperature (6 K) MB spectra collected in an applied field of 0.04 T for polycrystalline samples of **1a, 2a**, and [**3a**]SbF_6; the corresponding spectra of the ^{Ph2}TIP-based "**b** series" are provided in Figure S5. MB parameters summarized in Tables 3 and S3. Complex **1a** displays a single doublet with an isomer shift (δ) of 1.06 mm/s and quadrupole splitting (ΔE_Q) of 2.52 mm/s, consistent with the presence of a conventional high-spin Fe(II) center.[35] In contrast, the MB spectrum of [**1b**]OTf features two doublets in a ~2:1 ratio; the parameters for both species are typical of high-spin Fe(II) complexes: δ = 1.06 and 1.14 mm/s and ΔE_Q = 2.08 and 2.93 mm/s for the major and minor components, respectively. The two observed species likely correspond to conformational isomers of [**1b**]$^{+}$ that lie at different points along the continuum between square-pyramidal and trigonal-bipyramidal geometries. In support of this conclusion, the X-ray structure of [**1b**]$^{+}$ (*vide supra*) features two independent complexes in the unit cell with distinct τ-values of 0.60 and 0.55.

Chemistry, a European Journal, Vol. 19, No. 29 (July 2013): pg. 9686-9698. DOI.

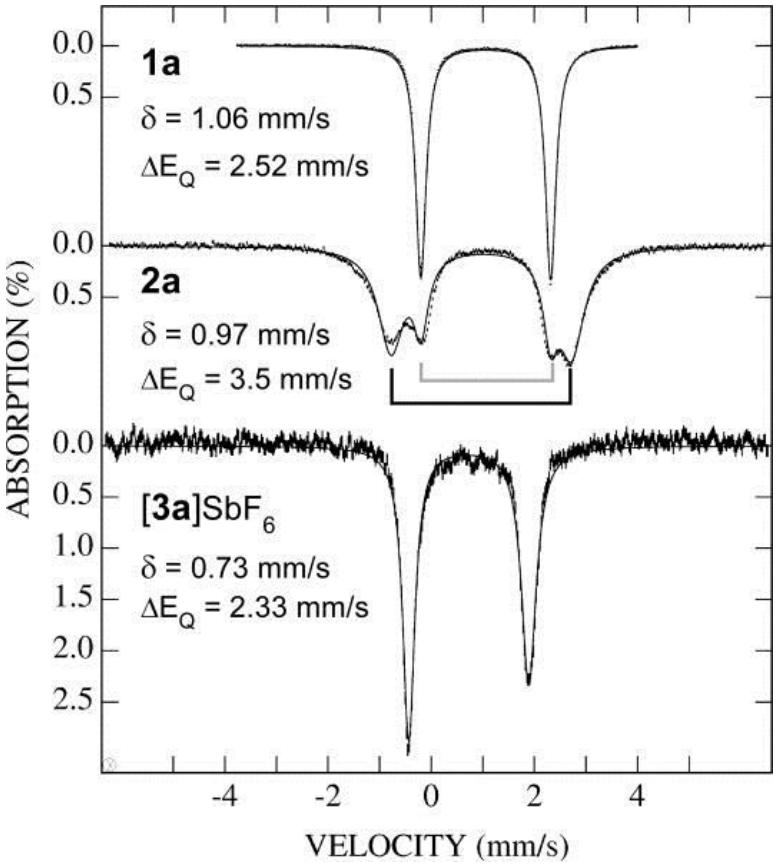

Figure 6 Mössbauer spectra of complexes **1a, 2a** and [**3a**]SbF_6 recorded at 6 K in an applied field of 0.04 T. The parameters indicated represent the principal species discussed in the text. The spectrum of sample **2a** contains a contribution from **1a**, amounting to 30% of the total Fe in the sample (inner doublet, indicated by the bracket). The spectrum of [**3a**]$^+$ shown in this figure was obtained by subtracting 20 % of impurities from the raw data.

The MB spectrum of **2a** exhibits a broad doublet with a large quadrupole splitting (δ = 0.97, ΔE_Q = 3.5 mm/s), although the presence of starting material (~30% of Fe) is also evident (Figure 6). Significantly, the modest decrease of 0.09 mm/s in isomer shift upon conversion of **1a** to **2a** provides unequivocal evidence that the oxidation is ligand-based, in support of the Fe^{2+}–ISQ formulation for **2a**. Likewise, the MB parameters of [**2b**]$^+$ are consistent with the presence of a high-spin Fe(II) center. In this case, proper fitting of the MB spectrum required three doublets with δ-values of 0.97 ± 0.02 mm/s and ΔE_Q values between 1.7–2.5 mm/s (Table S3). Given the nearly identical isomer shifts, these three species likely correspond to conformational isomers of [**2b**]$^+$, similar to the situation discussed

Chemistry, a European Journal, Vol. 19, No. 29 (July 2013): pg. 9686-9698. DOI.

above for [**1b**]$^{+}$. The heterogeneity observed in the [**2b**]$^{+}$ spectrum is related to the inability to prepare suitable crystals of this complex, which necessitated the use of powder samples lacking the intrinsic order of crystalline material. The broadness of the doublets for both **2a** and [**2b**]$^{+}$ is likely due to spin-spin relaxation effects.

MB spectra of [**3a**]$^{+}$ and [**3b**]$^{2+}$ each display a single doublet centered at δ = 0.73 and 0.64 mm/s, respectively, with quadrupole splittings of ~2.0 mm/s (Table 3; the [**3b**]$^{2+}$ spectrum also contains features arising from ferrous impurities). The lower δ-values suggest that one-electron oxidation of **2a**→[**3a**]$^{+}$ (or [**2b**]$^{+}$→[**3b**]$^{2+}$) involves significant removal of electron density from the Fe ions. However, the observed isomers shifts are larger than one would expect for high-spin Fe(III) centers, which typically display values between 0.4 and 0.6 mm/s.[35] A survey of high-spin [$Fe^{3+}(ISQ)_n$] complexes (n = 1, 2, or 3) prepared by Wieghardt and coworkers found δ-values ranging from 0.44 to 0.54 mm/s.[16-17] The MB data is therefore consistent with our DFT results that suggest *partial* IBQ character for the *O,N*-ligands in [**3a**]$^{+}$/[**3b**]$^{2+}$. It is also important to note that the **a**- and **b**-series of complexes yield very similar MB parameters, suggesting that the supporting ligand (^{Ph2}Tp(1-) vs. ^{Ph2}TIP) has little effect on the Fe/$L_{O,N}$ unit.

As shown in Table 3, isomer shifts derived from DFT calculations are quite consistent with the experimental data, although DFT generally underestimates δ-values by ~0.05-0.15 mm/s. In particular, DFT nicely reproduces the magnitude of changes (Δδ) across the **1**→**2**→**3** series. The overall agreement is less satisfactory for quadrupole splittings, but it is well-known that DFT has more difficulty computing accurate ΔE_Q values.[36] The general agreement between calculated and experimental MB parameters indicates that our computational models faithfully represent the electronic structures of these "redox-ambiguous" complexes.

2.C. Electronic Absorption and MCD Spectroscopies

The UV-vis-NIR spectra of **2a** and [**2b**]$^{+}$ displayed in Figure 2 are characterized by a broad absorption manifold (ε ~ 1.0 $mM^{-1}cm^{-1}$) centered around 750 nm (13,300 cm^{-1}). In this region, the **2a**/[**2b**]$^{+}$ spectra closely resemble those reported for other ISQ-containing

Chemistry, a European Journal, Vol. 19, No. 29 (July 2013): pg. 9686-9698. DOI.

complexes with various metal ions (Co^{3+}, Ni^{2+}, and Cu^{2+}),[37] as well as the spectrum measured by Carter *et al*. for a "free" ISQ radical.[38] These spectral similarities suggest that the transitions observed for **2a** and [**2b**]$^{+}$ are primarily ligand-based. This conclusion is also supported our time-dependent DFT (TD-DFT) calculations. The dominant contributor to the 750 nm feature is an intraligand transition in which the acceptor orbital is the SOMO of the ^{tBu}ISQ radical. TD-DFT calculations predict this transition to appear at 16,100 and 15,200 cm^{-1} for **2a** and [**2b**]$^{+}$, respectively (Table S4). In general, the TD-DFT methodology nicely replicates the energies and intensities of the experimental absorption features, as shown in Figure 7 for **2a** (electron density difference maps – EDDMs – for key transitions are provided in Figure S6). These calculations indicate that another component of the absorption manifold involves excitation to the ^{tBu}ISQ SOMO from an MO with mixed ^{tBu}ISQ/Fe(II) character; the computed energy for this transition is 15,000 cm^{-1} for **2a**. The weak near-infrared (NIR) bands evident for both complexes likely arise from Fe(II) d-d transitions, while features at higher energies (> 20,000 cm^{-1}) are attributed by TD-DFT to ^{tBu}ISQ→Fe(II) charge transfer (CT). These latter bands are relatively weak due to poor overlap between the ^{tBu}ISQ SOMO and half-occupied Fe(II) orbitals (Figure 5).

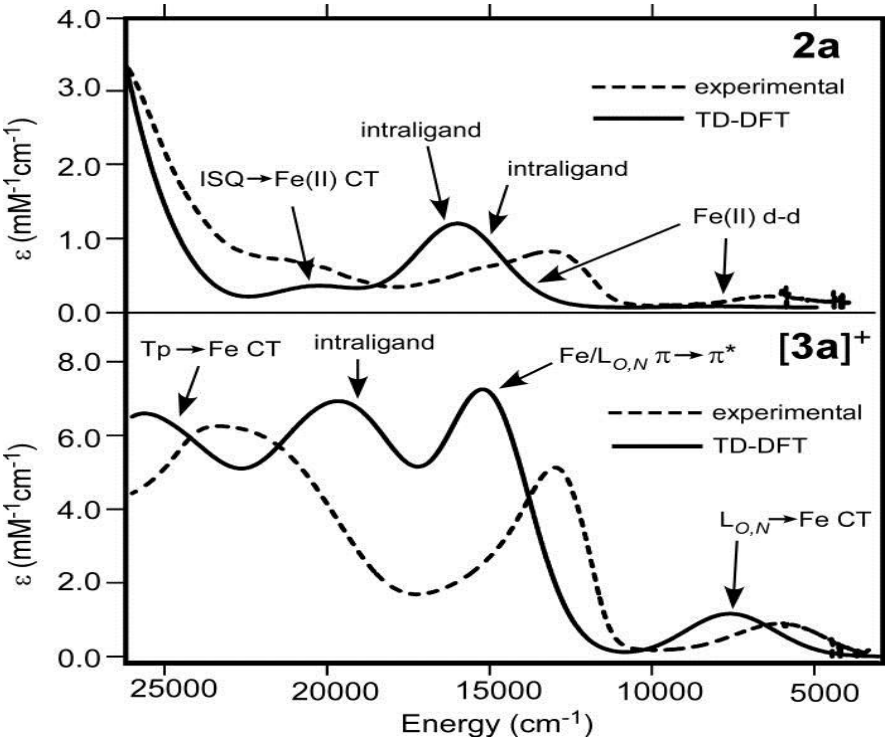

Chemistry, a European Journal, Vol. 19, No. 29 (July 2013): pg. 9686-9698. DOI.

Figure 7 Experimental (dashed line) and TD-DFT computed (solid line) absorption spectra for **2a** (top) and [**3a**]$^{+}$ (bottom). The arrows point to features in the computed spectra arising from the indicated type of electronic transition.

Analysis of the [**3a**]/[**3b**]$^{2+}$ spectra is more complex due to the large extent of mixing between Fe and ligand orbitals. For both complexes, the β-HOMO – containing approximately equal parts metal and ligand character (*vide supra*) – arises from a π-*bonding* interaction between the parent Fe 3d and $L_{O,N}$ orbitals (Figure 5). TD-DFT calculations, which again faithfully reproduce key features of the experimental spectrum (Figure 7 and Table S4), indicate that the intense absorption feature at ~13,000 cm^{-1} involves electron transfer from the β-HOMO to its unoccupied π-*antibonding* counterpart; therefore, this excitation is best described as a π→π* transition centered on the O1-Fe1-N7 unit. The broad band evident in the NIR region (ε ~ 1.0 mM^{-1}cm^{-1}) is then attributed to β-HOMO→Fe 3d transitions where the acceptor orbitals lack significant $L_{O,N}$ character. Given the mixed nature of the β-HOMO, this low-energy feature possesses both Fe d-d and LMCT character, as revealed in the EDDMs in Figure S7. Interestingly, the intraligand transition that is prominent at ~13,300 cm^{-1} in the **2a**/[**2b**]$^{+}$ spectra is calculated to appear at 18,900 cm^{-1} for [**3a**]$^{+}$, although this transition now contains some LMCT character. The blue-shift reflects the partial IBQ character of the *O,N*-coordinated ligands, since previous reports have demonstrated that the lowest-energy IBQ-based transition in metal complexes occurs near 20,800 cm^{-1}.[37] This intraligand transition is largely obscured in the [**3a**]$^{+}$ spectrum by intense N_{Tp}→Fe CT transitions. However, because the ^{Ph2}TIP-based MOs are greatly stabilized relative to their ^{Ph2}Tp counterparts (on account of the difference in charge), the N_{TIP}→Fe CT transitions are found at relatively high energies. Intraligand transitions are therefore evident in the 20,000-25000 cm^{-1} region of the [**3b**]$^{2+}$ spectrum with intensities of ~1.5 mM^{-1}cm^{-1}.

The electronic transitions of [**3b**](OTf)$_2$ were further probed through the collection of solid-state MCD spectra at low temperatures (4-30 K). All bands in the visible region exhibit temperature-dependent intensity characteristic of *C*-term behavior (Figure 7, top), as expected for a paramagnetic S = 2 species. Based on our analysis of the absorption spectrum, the most intense MCD feature at 12,500 cm^{-1} corresponds to the Fe/$L_{O,N}$ π→π* transition, while the bands centered

Chemistry, a European Journal, Vol. 19, No. 29 (July 2013): pg. 9686-9698. DOI.

around 20,000 cm^{-1} are ascribed primarily to intraligand transitions. Since MCD *C*-term intensity requires spin-orbit coupling between states, features that involve metal d-orbitals, such as ligand-field (d-d) and CT transitions, are relatively more intense in MCD than absorption spectra (*C/D* ratio).[39] Thus, the comparative weakness of the higher-energy features in the [**3b**]$^{2+}$ MCD spectrum is further confirmation of the ligand-based nature of these transitions.

Variable-temperature variable-field MCD (VTVH-MCD) data were collected at 790 nm (12660 cm^{-1}) for [**3b**]$^{2+}$. In these experiments, MCD intensity was monitored at five temperatures (2, 4, 8, 15, and 30 K) as the magnetic field (*H*) was varied from 0 to 7 T; by convention, the resulting magnetization curves are plotted against βH/2*k*T (Figure 8, bottom). As demonstrated by Solomon and Neese, quantitative analysis of the VTVH-MCD curves provides valuable information regarding spin-Hamiltonian parameters and transition polarizations.[40] The VTVH-MCD method is particularly powerful for non-Kramers systems, such as [**3b**]$^{2+}$, that are often inaccessible by EPR. The magnetization curves obtained at 790 nm saturate rapidly with field and exhibit very little "nesting" (*i.e.*, spread between curves obtained at different temperatures). Such behavior is characteristic of $S = 2$ systems with negative zero-field-splitting (ZFS).[41] Indeed, the best fit of the 790 nm data was obtained with $D = -5.0$ cm^{-1} and $E/D = 0.20$ (Figure 8), although a broad range of negative *D*-values (< 4 cm^{-1}) with moderate rhombicities ($0.1 < E/D < 0.25$) provided acceptable fits. Our analysis indicates that the corresponding transition is polarized in the *xz*-direction, which requires the *O,N*-donor ligand to lie in the *xz*-plane of the **D**-tensor (Figure 5).

Chemistry, a European Journal, Vol. 19, No. 29 (July 2013): pg. 9686-9698. DOI.

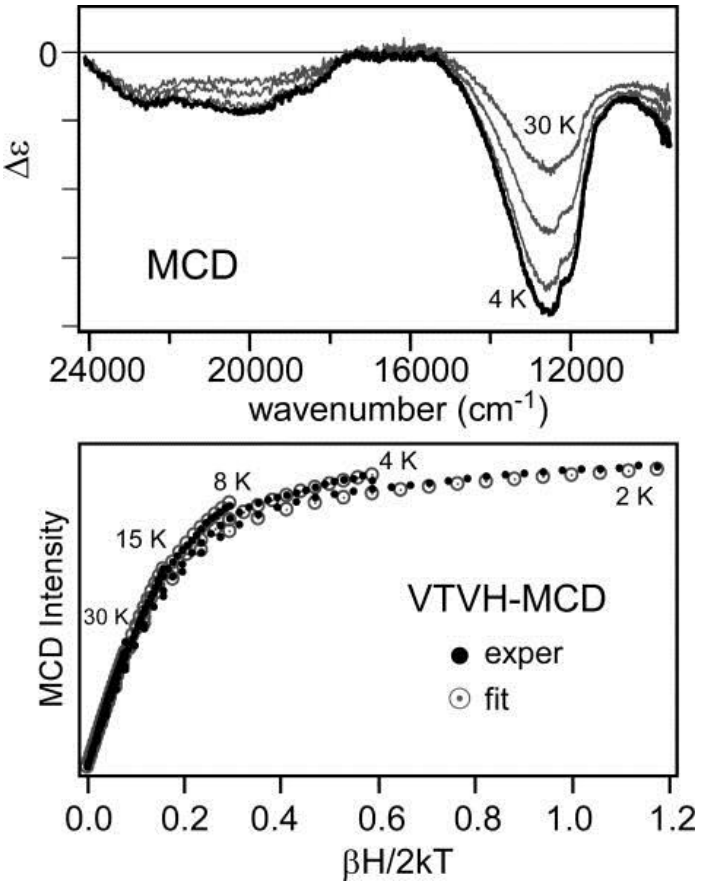

Figure 8 Top: Variable-temperature solid-state MCD spectra of [**3b**](OTf)$_2$. Spectra were measured at a magnetic field of 7 T and at temperatures of 4, 8, 15, and 30 K. Bottom: VTVH-MCD data collected at 790 nm for [**3b**](OTf)$_2$. Data were obtained at the indicated temperatures with magnetic fields (*H*) ranging from 0 to 7 T. The best fit (⊙) was obtained with the following spin Hamiltonian parameters: $S = 2$, $D = -5$ cm^{-1}, $E/D = 0.20$, $g_{iso} = 2.0$.

2.D. Resonance Raman Spectroscopies

Vibrational spectroscopy has proven valuable in the characterization of metal-bond phenoxyl and semiquinone radicals.[42] In the case of dioxolene complexes, the C–O stretching frequency is a sensitive indicator of ligand oxidation state, ranging from 1400-1500 cm^{-1} for semiquinones and 1620-1640 cm^{-1} for benzoquinones.[43] By contrast, the vibrational features of iminobenzo(semi)quinones have not been examined in detail. We therefore collected resonance Raman spectra on frozen samples of [**3a**]SbF_6 in CD_2Cl_2 (Figure 9). The experiments utilized 488 nm laser excitation, in resonance with the

Chemistry, a European Journal, Vol. 19, No. 29 (July 2013): pg. 9686-9698. DOI.

intraligand transitions that appear in this region (*vide supra*). To aid in peak assignments, we prepared a sample of [**3a**]$^+$ in which the *O,N*-ligand was labeled with the ^{15}N isotope; the difference spectrum revealed several peaks that are sensitive to ^{15}N substitution (Figure 9). Interpretation of the rRaman data was further aided by DFT frequency calculations employing the BP functional.

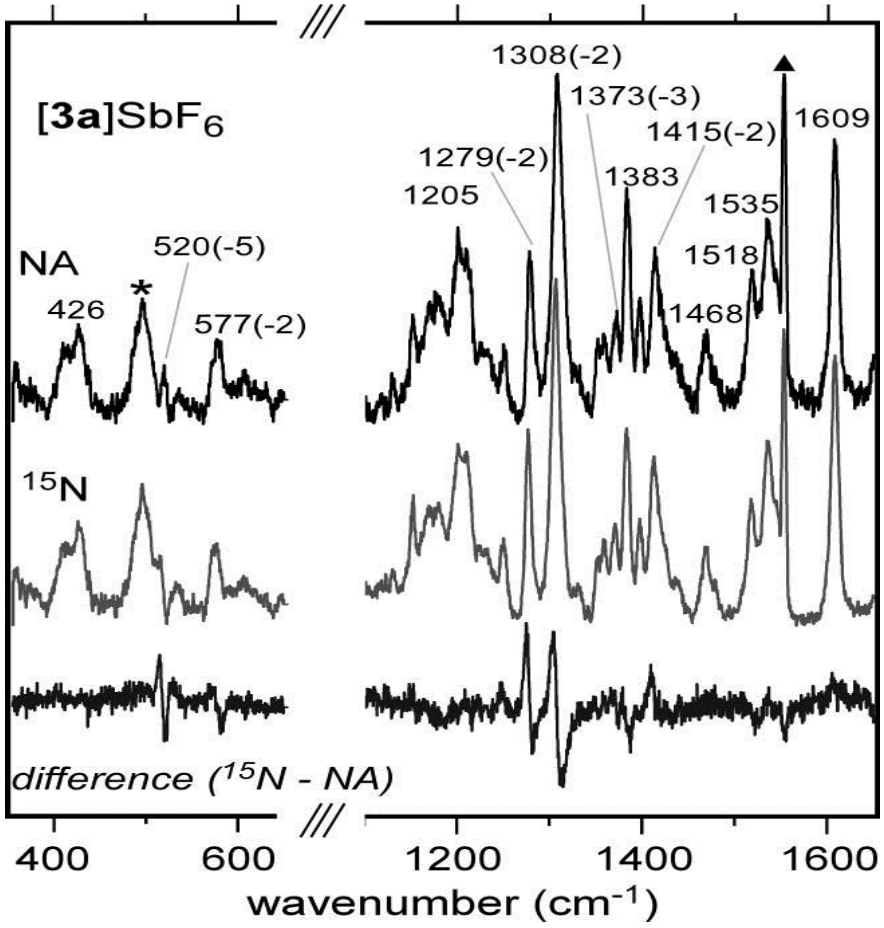

Figure 9 Resonance Raman spectra obtained with 488.0 nm excitation (45 mW) of frozen CD_2Cl_2 solutions of (top) natural abundance [**3a**]SbF_6, and (middle) [**3a**]SbF_6 with incorporation of ^{15}N isotope in the $L_{O,N}$ ligand. The difference spectrum is shown on the bottom. Frequencies (in cm^{-1}) are provided for selected peaks, with the corresponding $^{14}N \rightarrow {}^{15}N$ shifts shown in parenthesis. Peaks marked with an asterisk (*) arise from the frozen solvent, while the peak marked with a triangle arises from condensed liquid O_2.

Based on literature precedents involving metal-semiquinone complexes,[42c, 42d] the two isotopically-sensitive peaks at 520 and 577 cm^{-1} in the [**3a**]$^+$ spectrum are attributed to motions of the five-

Chemistry, a European Journal, Vol. 19, No. 29 (July 2013): pg. 9686-9698. DOI.

membered chelate ring formed by the Fe center and *O,N*-ligand. In support of this assignment, DFT predicts two modes at 532 and 588 cm^{-1} (with ^{15}N isotope shifts of 7 and 4 cm^{-1}, respectively) with large degrees of chelate stretching character. The mode at 520 cm^{-1} (calculated at 532 cm^{-1}) is best described as a chelate breathing mode, whereas the chelate vibrations in the higher-energy mode are strongly mixed with intraligand C-C bond movements. Graphical depictions of these normal modes, along with further information concerning the computed vibrational spectrum, are provided in Figure S8.

The [**3a**]$^{+}$ spectrum exhibits numerous peaks in the 1100-1650 cm^{-1} region. These features are not present in the rR spectrum of **1a** (Figure S9); we therefore conclude that they arise from the oxidized *O,N*-ligand (an exception is the 1609 cm^{-1} peak, which appears in both spectra). Studies of analogous semiquinone complexes[42c, 42d] found that the most intense peaks in this region correspond to modes that couple O-C stretching and C-C ring motions. Indeed, DFT predicts two ν(O-C)-based modes for [**3a**]$^{+}$ at 1342 and 1404 cm^{-1} that are slightly sensitive to ^{15}N-substitution (calculated shifts of ~1 cm^{-1}). These modes likely corresponding to the prominent peaks at 1308 and 1383 cm^{-1} in the experimental spectrum. Modes with significant ν(N-C) character have computed frequencies of 1319, 1384, and 1495 cm^{-1}, with ^{15}N isotope shifts of ~1-3 cm^{-1} in each case. The two lower-energy modes nicely match the experimental peaks at 1279 and 1373 cm^{-1}, respectively, while the higher-energy mode is not observed.

Vibrational frequency calculations were also performed for the **Ga-ISQ** and **Ga-IBQ** models, which possess *O,N*-ligands with unambiguous oxidation states (*vide supra*). DFT predicts two ν(O-C) modes at 1319 and 1424 cm^{-1} for **Ga-ISQ**, while the corresponding modes for **Ga-IBQ** possess much higher frequencies of 1540 and 1584 cm^{-1}. Since the putative ν(O-C) modes of [**3a**]$^{+}$ have experimental energies of 1308 and 1383 cm^{-1}, the rRaman data appear to support an ISQ assignment for the ligand oxidation state.

Chemistry, a European Journal, Vol. 19, No. 29 (July 2013): pg. 9686-9698. DOI.

Discussion

A variety of spectroscopic and computational methods have been employed to evaluate the electronic structures of mononuclear Fe complexes bound to redox-active ligands derived from 2-amino-4,6-di-*tert*-butylphenol ($^{tBu}APH_2$). Our studies included the ^{Ph2}Tp-supported complexes **2a** and [**3a**]SbF_6 (previously reported), as well as a parallel "**b**-series" of complexes prepared with the neutral ^{Ph2}TIP supporting ligand (Scheme 2). The results described here strongly support our earlier conclusion – made on the basis of XRD and EPR data – that **2a** contains a high-spin Fe(II) center antiferromagnetically coupled to an ISQ^{tBu} ligand radical (overall spin of 3/2). Specifically, the presence of a ferrous ion in **2a** was verified by MB spectroscopy (δ = 0.97), and the unique absorption features were shown to arise from ^{tBu}ISQ ligand-based transitions. Although we were not able to obtain a crystal structure of [**2b**]$^+$, similarities between the spectral properties of **2a** and [**2b**]$^+$ indicate that the complexes share identical electronic configurations. Analysis of the more-oxidized [**3a**]$^+$ and [**3b**]$^{2+}$ species is less straightforward, since a preponderance of the data indicate that actual electronic structures lie between the Fe^{3+}–ISQ and Fe^{2+}–IBQ limits. For instance, the *O,N*-ligand in the [**3b**]$^{2+}$ crystal structure exhibits a more pronounced quinoid distortion than expected for a typical ISQ ligand, and the isomer shifts measured for [**3a**]$^+$ and [**3b**]$^{2+}$ ($\delta_{ave} \sim 0.68$) are considerably outside the range expected for high-spin ferric ions. However, the v(C-O) frequencies observed by rRaman spectroscopy are more consistent with an ISQ oxidation state.

The unprecedented example of an Fe(II) center bound to an ISQ radical in complexes **2a** and [**2b**]$^+$ is made possible by the combination of high-spin states and trigonal-bipyramidal 5C geometries, which result in Fe centers with enhanced electron affinities. Concerning the role of spin state, our DFT calculations indicate that isomers of **2a** with intermediate- or low-spin centers converge to the alternate Fe^{3+}–amidophenolate(2-) configuration. And the importance of coordination number is highlighted by comparison to the six-coordinate (6C) [$(L_{N4})Fe^{3+}$(ISQ)]$^{2+}$ complexes prepared by Wieghardt (where L_{N4} = *cis*-cyclam or tren).[16] These complexes undergo only ligand-based reductions to give the corresponding Fe(III) species with closed-shell amidophenolate(2-) ligands, even when the Fe center is high-spin.[44] These insights have implications for the

Chemistry, a European Journal, Vol. 19, No. 29 (July 2013): pg. 9686-9698. DOI.

Fe/O_2/substrate intermediate in the catalytic cycle of APDOs. Like **2a**/[**2b**]$^+$, this species contains a high-spin center, yet it also has a 6C geometry due to the presence of the O_2 ligand. Thus, extrapolation from the synthetic models would seem to favor the closed-shell electronic structure of intermediate **I** in Scheme 1. However, unlike Wieghardt's $[(L_{N4})Fe^{3+}(ISQ)]^{2+}$ models, the sixth ligand in the enzymatic intermediate (i.e., superoxide) is redox-active and electron-withdrawing, and therefore capable of facilitating electron-transfer from the substrate ligand to the Fe center. We are currently examining the reactivity of our Fe^{2+}–APH and Fe^{2+}–ISQ complexes with O_2 and NO to assess the impact of small molecule binding on the electronic configuration of the $Fe/L_{O,N}$ unit.

Finally, it is worthwhile to consider why complexes like **2a**/[**2b**]$^+$ are viable whereas the corresponding Fe(II)–SQ complexes have not been reported despite extensive efforts in modeling catechol dioxygenases. Indeed, a catecholate analogue of **2a** has already been reported and crystallographically characterized by Moro-oka, namely, $[Fe^{2+}(^{tBu,iPr}Tp)(DBC)]$ (**5**; where DBC = dianion of 3,5-di-*tert*-butylcatechol).[45] Like **2a**, complex **5** contains a trigonal bipyramidal Fe/Tp unit bound to a bidentate "substrate" ligand; however, the catecholate lacks quinoid distortion (C-O bond distances of 1.35 and 1.38 Å), and the collective metric and spectroscopic data demand an Fe(III)-catecholate description. The divergent electronic structures of **2a** and **5** point to the intrinsic difference in redox potentials between catecholate and amidophenolate dianions. This difference may have mechanistic implications for the ring-cleaving dioxygenases. Normally, it is assumed that ECDOs and APDOs share a common catalytic mechanism; however, our synthetic experience indicates that a species like intermediate **II** in Scheme 1 is more feasible for APDOs than ECDOs. Thus, the two catalytic cycles may differ at this point, with the ECDOs adopting an intermediate **I** structure (as proposed by Ye and Neese[25]) and the APDOs adopting an intermediate **II** structure with considerable radical character on the substrate.

Chemistry, a European Journal, Vol. 19, No. 29 (July 2013): pg. 9686-9698. DOI.

Experimental Section

Materials and physical methods

All reagents and solvents were purchased from commercial sources and used as received, unless otherwise noted. Acetonitrile, dichloromethane, and tetrahydrofuran were purified and dried using a Vacuum Atmospheres solvent purification system. The synthesis and handling of air-sensitive materials were performed under inert atmosphere using a Vacuum Atmospheres Omni-Lab glovebox. The ligands K(^{Ph2}Tp),[46] ^{Ph2}TIP,[28] and ^{tBu}APH$_2$[47] were prepared according to literature procedures. ^{15}N-labeled ^{tBu}APH$_2$ was prepared using ^{15}NH$_4$OH purchased from Cambridge Isotopes. Elemental analyses were performed at Midwest Microlab, LLC in Indianapolis, IN.

Samples of **[2b**]OTf for spectroscopic studies were prepared by treating [**1b**]OTf with one equivalent of TTBP$^{\bullet}$[48] in CH_2Cl_2. After stirring for two hours, the green solution was filtered and the solvent removed under vacuum. The resulting powder exhibited the following peaks in the IR spectrum: 3342 [v(N-H)], 3054, 1439, 1259, 1222 cm^{-1}.

Spectroscopic Methods UV-vis absorption spectra were obtained with an Agilent 8453 diode array spectrometer; NIR absorption spectra were measured using an Agilent Cary 5000 spectrophotometer. Fourier-transform infrared (FTIR) spectra of solid samples were measured with a Thermo Scientific Nicolet iS5 FTIR spectrometer equipped with the iD3 attenuated total reflectance accessory. EPR experiments were performed using a Bruker ELEXSYS E600 equipped with an ER4415DM cavity resonating at 9.63 GHz, an Oxford Instruments ITC503 temperature controller, and an ESR-900 He flow cryostat. MCD spectra were obtained using a Jasco J-715 spectropolarimeter in conjunction with an Oxford Instruments SM-4000 8T magnetocryostat. Solid-state samples of [**3a**]SbF_6 were prepared as uniform mulls in fluorolube. All MCD spectra were obtained by subtracting the -7 T spectrum from the +7 T spectrum to eliminate potential artifacts. Resonance Raman spectra were measured using 488.0 nm excitation from a Spectra Physics Ar$^+$ laser (model 2025-05), with 45 mW at the sample point in a 180° backscattering geometry. The sample was placed in a transparent quartz Dewar cell

Chemistry, a European Journal, Vol. 19, No. 29 (July 2013): pg. 9686-9698. DOI.

filled with liquid nitrogen and spun at 800 rpm. Spectra were collected with the Spec-10 system (Princeton Instruments) installed on the 1269 spectrograph (SPEX Industries) equipped with a standard 1200 grove/inch grating at 80 mm slit width. Spectra were calibrated with fenchone and indene standards. Low-field (0.04 T) variable temperature (5 K – 200 K) Mössbauer spectra were recorded on a closed-cycle refrigerator spectrometer, model CCR4K, equipped with a 0.04 T permanent magnet, maintaining temperatures between 5 and 300 K. Mössbauer spectra were analyzed using the software WMOSS (Thomas Kent, SeeCo.us, Edina, Minnesota). The samples were polycrystalline powders, suspended in nujol, placed in Delrin 1.00 mL cups and frozen in liquid nitrogen. The isomer shifts are quoted at 6 K with respect to iron metal spectra recorded at 298 K.

Electrochemical measurements Cyclic voltammetric (CV) measurements were conducted in the glovebox with an epsilon EC potentiostat (iBAS) at a scan rate of 100 mV/s with 100 mM $(NBu_4)PF_6$. A three-electrode cell containing a Ag/AgCl reference electrode, a platinum auxiliary electrode, and a glassy carbon working electrode was employed. Under these conditions, the ferrocene/ferrocenium ($Fc^{+/0}$) couple has an $E_{1/2}$ value of +0.52 V in CH_2Cl_2.

Synthesis of Fe complexes

Synthetic procedures for complexes **1a, 2a**, and [**3a**]SbF_6 were previously published in Bittner *et al*.[26]

[(^{Ph2}TIP)Fe^{2+}(^{tBu}APH)]X ([**1b**]X; X = OTf, BPh_4): [(^{Ph2}TIP)$Fe^{2+}(CH_3CN)_3$](OTf)$_2$[22] (1.12 g, 0.927 mmol) and $^{tBu}APH_2$ (205.1 mg, 0.927 mmol) were mixed in CH_2Cl_2 (10 mL), followed by addition of triethylamine (142 µL, 1.02 mmol). After stirring overnight, the reaction was filtered and the solvent removed under vacuum. The brown solid was taken up in toluene and the product precipitated with excess pentane. The yellow solid was collected, washed again with pentane, and then dried to yield [**1b**]OTf as a bright yellow powder (yield = 921 mg, 86%). IR (solid): $\tilde{\nu}$ = 3348, 3059, 2949, 2901, 2861, 1064, 1462, 1442, 1273, 1255, 1152, 1030 cm^{-1}. Counteranion metathesis was performed by mixing [**1b**]OTf (125 mg, 0.108 mmol) with $NaBPh_4$ (37.6 mg, 0.110 mmol) in MeOH (3 mL). After stirring for

Chemistry, a European Journal, Vol. 19, No. 29 (July 2013): pg. 9686-9698. DOI.

15 minutes, a yellow precipitate formed that was collected and dried under vacuum. X-ray quality crystals of [**1b**]BPh_4 were obtained by layering a concentrated 1,2-dichloroethane (DCE) solution with MeOH (yield = 83.1 mg, 48%). IR (solid): 3340, 3050, 2948, 2863, 1578, 1478, 1443, 1379, 1305, 1264, 1142, 1074, 1023 cm^{-1}. UV/Vis (CH_2Cl_2): λ_{max} (ε) = 815 (10), 399 (1160 $M^{-1}cm^{-1}$). The X-ray structure revealed three uncoordinated DCE molecules in the asymmetric unit, and elemental analysis suggests that a small amount of solvent (~0.3 equiv./Fe) remains after drying. Elemental analysis calcd (%) for $C_{86}H_{81}BFeN_7OP$•0.3DCE: C 76.70, H 6.11, N 7.23; found: C 76.70, H 6.13, N 7.13.

[(^{Ph2}TIP)Fe^{3+}(^{tBu}ISQ)]$(OTf)_2$ ([**3b**]OTf_2): Complex [**1b**]OTf (184 mg, 0.159 mmol) and two equiv. of AgOTf (83 mg, 0.32 mmol) were stirred in THF (6 mL) for one hour, yielding a dark green solution. The solution was filtered through celite and the solvent removed under vacuum. The resulting solid was taken up in CH_2Cl_2 (or 1,2-dichloroethane) and layered with *n*-hexane, providing dark green needles suitable for XRD experiments (yield = 208 mg, 94%). IR (solid): 3270, 3058, 2959, 1603, 1578, 1469, 1445, 1364, 1257, 1221, 1147, 1073, 1026 cm^{-1}. UV/Vis (CH_2Cl_2): λ_{max} (ε) = 798 nm (2800 $M^{-1}cm^{-1}$). Elemental analysis calcd (%) for $C_{64}H_{60}F_6FeN_7O_7PS_2$: C 58.94, H 4.64, N 7.52; found: C 54.88, H 4.84, N 6.79. The disagreement indicates that small amounts of impurities and/or solvent are present.

[(^{Ph2}Tp)Fe^{2+}(DMAPH)] (**4a**): 2-(dimethylamino)-4,6-di-*tert*-butylphenol (DMAPH) was prepared according to the previously published procedure.[49] $Fe(OTf)_2$ (248 mg, 0.701 mmol), K(^{Ph2}Tp) (497 mg, 0.701 mmol), and DMAPH (175 mg, 0.701 mmol) were mixed in a 2:1 solution of CH_2Cl_2:MeCN (15 mL), followed by addition of triethylamine (108 µL, 0.774 mmol). After stirring for several hours, the solvent was removed. The resulting solid was taken up in CH_2Cl_2 (6 mL) and filtered. Storage of this solution in a freezer (−30 °C) for several days provided bright yellow crystals suitable for X-ray crystallographic analysis (yield = 160 mg, 24%). IR (solid): 3056, 2948, 2855, 2637, 1545, 1462, 1412, 1356, 1302, 1264, 1246, 1167, 1060, 1028, 1007 cm^{-1}. UV/Vis (CH_2Cl_2): λ_{max} (ε) = 365 nm (1950 $M^{-1}cm^{-1}$). Elemental analysis calcd (%) for $C_{61}H_{60}BFeN_7O$: C, 75.23; H, 6.21; N, 10.07; found: C, 74.97; H, 6.18; N, 10.07.

Chemistry, a European Journal, Vol. 19, No. 29 (July 2013): pg. 9686-9698. DOI.

Crystallographic studies

X-ray diffraction (XRD) data were collected with an Oxford Diffraction SuperNova kappa-diffractometer (Agilent Technologies) equipped with dual microfocus Cu/Mo X-ray sources, X-ray mirror optics, Atlas CCD detector, and low-temperature Cryojet device. The data were processed with CrysAlis Pro program package (Agilent Technologies, 2011) typically using a numerical Gaussian absorption correction (based on the real shape of the crystal), followed by an empirical multi-scan correction using SCALE3 ABSPACK routine. The structures were solved using SHELXS program and refined with SHELXL program[50] within Olex2 crystallographic package.[51] B- and C-bonded hydrogen atoms were positioned geometrically and refined using appropriate geometric restrictions on the corresponding bond lengths and bond angles within a riding/rotating model (torsion angles of methyl hydrogens were optimized to better fit the residual electron density).

Crystal data for [**1b**](BPh$_4$)·1.5 DCE: Formula= $C_{89}H_{87}BCl_3FeN_7OP$; M_w= 1474.68; triclinic; space group $P-1$; a= 17.3220(4), b= 20.6267(4), c= 22.0768(4) Å; α= 81.955(2), β= 78.343(2), γ= 87.958(2)°; V= 7649.0(3) Å^3; T = 100 K; Z= 4; 101066 reflections measured; 37578 unique reflections (R_{int} = 0.0357) ; final R indices [$I>2\sigma(I)$] $R1$= 0.0552 and $wR2$= 0.1469; R indices (all data) $R1$=0.0708 and $wR2$=0.1608.

Crystal data for [**3b**](OTf)$_2$·CH_2Cl_2: Formula= $C_{65}H_{62}Cl_2F_6FeN_7O_7PS_2$; M_w = 1389.08; monoclinic; space group $P2_1/c$; a= 20.0160(13), b= 15.3008(11), c= 22.2057(18) Å; α= 90, β= 94.320(8), γ= 90°; V= 6781.4(9) Å^3; T= 100 K; Z= 4; 35453 reflections measured; 13347 unique reflections (R_{int} = 0.0787); final R indices [$I>2\sigma(I)$] $R1$=0.0723 and $wR2$=0.1786; R indices (all data) $R1$=0.1153 and $wR2$=0.2105.

Crystal data for [**4a**]·4CH_2Cl_2: Formula= $C_{65}H_{68}BCl_8FeN_7$; M_w= 1313.56; monoclinic; space group $P2_1/c$; a= 17.1045(5), b= 14.4938(5), c= 26.5165(8) Å; α= 90, β= 100.482(3), γ= 90°; V=6464.0(3) Å^3; T = 100 K; Z= 4; 41153 reflections measured; 12682 unique reflections (R_{int}= 0.0356); final R indices [$I>2\sigma(I)$]

Chemistry, a European Journal, Vol. 19, No. 29 (July 2013): pg. 9686-9698. DOI.

*R*1=0.0606 and *wR*2=0.1488; *R* indices (all data) *R*1=0.0764 and *wR*2=0.1588.

DFT calculations

DFT calculations were performed using the ORCA 2.8 software package developed by Dr. F. Neese.[52] Geometry optimizations employed either the Becke-Perdew (BP86) functional[53] or Becke's three-parameter hybrid functional for exchange along with the Lee-Yang-Parr correlation functional (B3LYP).[54] Ahlrichs' valence triple-ζ basis set (TZV), in conjunction with the TZV/J auxiliary basis set,[55] were used for all calculations. Time-dependent DFT (TD-DFT) calculations[56] computed absorption energies and intensities within the Tamm-Dancoff approximation.[57] In each case, at least 60 excited states were calculated. Vibrational frequency calculations were performed with a truncated [**3a**]$^+$ model with hydrogen atoms at the 3- and 5-positions of the Tp ligand. Calculation of the harmonic force fields proved that the optimized structure is a local minima on the potential energy surface. MB parameters were calculated using the approach described in Römelt *et al*.[58]; in these calculations, the size of the integration grid for Fe, O, and N atoms was increased. The gOpenMol program[59] developed by Laaksonen was used to generate isosurface plots of molecular orbitals.

Acknowledgements

We are grateful to Dr. Kazimierz Czarnecki and Prof. James Kincaid (Marquette Univ.) for the collection of resonance Raman data. We also thank Dr. Brian Bennett for allowing us to measure EPR data at the National Biomedical EPR Center (supported by NIH P41 Grant EB001980), and Thomas Brunold (Univ. Wisconsin – Madison) for access to his MCD instrument. This research is generously supported by the National Science Foundation (CAREER CHE-1056845 to A.T.F, CHE-0956779 to C.V.P).

References

1. **a.** Costas M, Mehn MP, Jensen MP, Que L. Chem. Rev. 2004;104:939–986.
b. Solomon EI, Brunold TC, Davis MI, Kemsley JN, Lee SK, Lehnert N, Neese F, Skulan AJ, Yang YS, Zhou J. Chem. Rev. 2000;100:235–349.

c. Gibson DT, Parales RE. Curr. Opin. Biotechnol. 2000;11:236–243.
d. Vaillancourt FH, Bolin JT, Eltis LD. Crit. Rev. Biochem. Mol. Biol. 2006;41:241–267.
e. Kovaleva EG, Lipscomb JD. Nat. Chem. Biol. 2008;4:186–193.

2. **a.** Lipscomb JD, Orville AM. In: Met. Ions Biol. Syst. Sigel H, Sigel A, editors. Vol. 28. Marcel Dekker; New York: 1992. pp. 243–298.
b. Que L, Jr., Ho RYN. Chem. Rev. 1996;96:2607–2624.
c. Kovaleva EG, Neibergall MB, Chakrabarty S, Lipscomb JD. Acc. Chem. Res. 2007;40:475–483.

3. **a.** Li XW, Guo M, Fan J, Tang WY, Wang DQ, Ge HH, Rong H, Teng MK, Niu LW, Liu Q, Hao Q. Protein Sci. 2006;15:761–773.
b. Lendenmann U, Spain JC. J. Bacteriol. 1996;178:6227–6232.

4. **a.** Harpel MR, Lipscomb JD. J. Biol. Chem. 1990;265:22187–22196.
b. Veldhuizen EJA, Vaillancourt FH, Whiting CJ, Hsiao MMY, Gingras G, Xiao YF, Tanguay RM, Boukouvalas J, Eltis LD. Biochem. J. 2005;386:305–314.
c. Titus GP, Mueller HA, Burgner J, de Cordoba SR, Penalva MA, Timm DE. Nat. Struct. Biol. 2000;7:542–546.
d. Machonkin TE, Doerner AE. Biochemistry. 2011;50:8899–8913.
e. Machonkin TE, Holland PL, Smith KN, Liberman JS, Dinescu A, Cundari TR, Rocks SS. J. Biol. Inorg. Chem. 2010;15:291–301.
f. Xu L, Resing K, Lawson SL, Babbitt PC, Copley SD. Biochemistry. 1999;38:7659–7669.
g. Yin Y, Zhou NY. Curr. Microbiol. 2010;61:471–476.

5. **a.** Matera I, Ferraroni M, Buerger S, Scozzafava A, Stolz A, Briganti F. J. Mol. Biol. 2008;380:856–868.
b. Hintner JP, Remtsma T, Stolz A. J. Biol. Chem. 2004;279:37250–37260.
c. Hintner JP, Lechner C, Riegert U, Kuhm AE, Storm T, Reemtsma T, Stolz A. J. Bacteriol. 2001;183:6936–6942.

6. Denisov IG, Makris TM, Sligar SG, Schlichting I. Chem. Rev. 2005;105:2253–2278.

7. Tinberg CE, Lippard SJ. Acc. Chem. Res. 2011;44:280–288.

8. Krebs C, Fujimori DG, Walsh CT, Bollinger JM. Acc. Chem. Res. 2007;40:484–492.

9. **a.** Lipscomb JD. Curr. Opin. Struct. Biol. 2008;18:644–649.
b. Bugg TDH, Ramaswamy S. Curr. Opin. Chem. Biol. 2008;12:134–

140.
c. Zhang Y, Colabroy KL, Begley TP, Ealick SE. Biochemistry. 2005;44:7632–7643.

10. Kovaleva EG, Lipscomb JD. Science. 2007;316:453–457.

11. Arciero DM, Lipscomb JD. J. Biol. Chem. 1986;261:2170–2178.

12. Sanvoisin J, Langley GJ, Bugg TDH. J. Am. Chem. Soc. 1995;117:7836–7837.

13. **a.** Pierpont CG. Inorg. Chem. 2011;50:9766–9772.
b. Pierpont CG. Coord. Chem. Rev. 2001;219:415–433.
c. Koch WO, Schunemann V, Gerdan M, Trautwein AX, Kruger HJ. Chem. Eur. J. 1998;4:1255–1265.

14. **a.** Das D, Sarkar B, Mondal TK, Mobin SM, Fiedler J, Kaim W, Lahiri GK. Inorg. Chem. 2011;50:7090–7098.
b. Hubner R, Sarkar B, Fiedler J, Zalis S, Kaim W. Eur. J. Inorg. Chem. 2012:3569–3576.
c. Das AK, Sarkar B, Duboc C, Strobel S, Fiedler J, Zalis S, Lahiri GK, Kaim W. Angew. Chem. Intl. Ed. 2009;48:4242–4245.
d. Das D, Das AK, Sarkar B, Mondal TK, Mobin SM, Fiedler J, Zalis S, Urbanos FA, Jimenez-Aparicio R, Kaim W, Lahiri GK. Inorg. Chem. 2009;48:11853–11864.

15. **a.** Min KS, Weyhermuller T, Wieghardt K. Dalton Trans. 2004:178–186.
b. Mukherjee S, Weyhermuller T, Bill E, Wieghardt K, Chaudhuri P. Inorg. Chem. 2005;44:7099–7108.

16. **a.** Chun HP, Bill E, Weyhermuller T, Wieghardt K. Inorg. Chem. 2003;42:5612–5620.
b. Chun H, Bill E, Bothe E, Weyhermuller T, Wieghardt K. Inorg. Chem. 2002;41:5091–5099.

17. **a.** Chun H, Verani CN, Chaudhuri P, Bothe E, Bill E, Weyhermuller T, Wieghardt K. Inorg. Chem. 2001;40:4157–4166.
b. Chun H, Weyhermuller T, Bill E, Wieghardt K. Angew. Chem. Intl. Ed. 2001;40:2489–2492.

18. **a.** Blackmore KJ, Sly MB, Haneline MR, Ziller JW, Heyduk AF. Inorg. Chem. 2008;47:10522–10532.
b. Blackmore KJ, Ziller JW, Heyduk AF. Inorg. Chem. 2005;44:5559–5561.

19. Poddel'sky AI, Cherkasov VK, Abakumov GA. Coord. Chem. Rev. 2009;253:291–324.

20. Spence EL, Langley GJ, Bugg TDH. J. Am. Chem. Soc. 1996;118:8336–8343.

21. **a.** Georgiev V, Borowski T, Siegbahn PEM. J. Biol. Inorg. Chem. 2006;11:571–585.
b. Bassan A, Borowski T, Siegbahn PEM. Dalton Trans. 2004:3153–3162.
c. Siegbahn PEM, Haeffner F. J. Am. Chem. Soc. 2004;126:8919–8932.

22. Emerson JP, Kovaleva EG, Farquhar ER, Lipscomb JD, Que L. Proc. Natl. Acad. Sci. U.S.A. 2008;105:7347–7352.

23. Mbughuni MM, Chakrabarti M, Hayden JA, Bominaar EL, Hendrich MP, Munck E, Lipscomb JD. Proc. Natl. Acad. Sci. U.S.A. 2010;107:16788–16793.

24. Mbughuni MM, Chakrabarti M, Hayden JA, Meier KK, Dalluge JJ, Hendrich MP, Munck E, Lipscomb JD. Biochemistry. 2011;50:10262–10274.

25. Christian GJ, Ye SF, Neese F. Chem. Sci. 2012;3:1600–1611.

26. Bittner MM, Lindeman SV, Fiedler AT. J. Am. Chem. Soc. 2012;134:5460–5463.

27. **a.** Koehntop KD, Emerson JP, Que L. J. Biol. Inorg. Chem. 2005;10:87–93.
b. Burzlaff N. Angew. Chem. Intl. Ed. 2009;48:5580–5582.

28. Bittner MM, Baus JS, Lindeman SV, Fiedler AT. Eur. J. Inorg. Chem. 2012:1848–1856.

29. Addison AW, Rao TN, Reedijk J, Vanrijn J, Verschoor GC. J. Chem. Soc., Dalton Trans. 1984:1349–1356.

30. Brown SN. Inorg. Chem. 2012;51:1251–1260.

31. For reasons that are not clear to us, the ^{Ph2}TIP-based complexes failed to exhibit well-defined electrochemical events.

32. Our use of the broken-symmetry DFT approach to examine metal-radical interactions is indebted to the pioneering work of Frank Neese and coworkers

33. **a.** Yamaguchi K, Takahara Y, Fueno T. In: Applied Quantum Chemistry. Smith VH, editor. Reidel; Dordrecht: 1986. p. 155.
b. Soda T, Kitagawa Y, Onishi T, Takano Y, Shigeta Y, Nagao H, Yoshioka Y, Yamaguchi K. Chem. Phys. Lett. 2000;319:223–230.

34. Pau MYM, Davis MI, Orville AM, Lipscomb JD, Solomon EI. J. Am. Chem. Soc. 2007;129:1944–1958.

35. Münck E. In: Physical Methods in Bioinorganic Chemistry. Spectroscopy and Magnetism. Que L Jr., editor. University Science Books; Sausalito, CA: 2000. pp. 287–319.

36. **a.** Ye SF, Price JC, Barr EW, Green MT, Bollinger JM, Krebs C, Neese F. J. Am. Chem. Soc. 2010;132:4739–4751.
b. Sinnecker S, Svensen N, Barr EW, Ye S, Bollinger JM, Neese F, Krebs C. J. Am. Chem. Soc. 2007;129:6168–6179.
c. Godbout N, Havlin R, Salzmann R, Debrunner PG, Oldfield E. J. Phys. Chem. A. 1998;102:2342–2350.

37. **a.** Chaudhuri P, Verani CN, Bill E, Bothe E, Weyhermuller T, Wieghardt K. J. Am. Chem. Soc. 2001;123:2213–2223.
b. Min KS, Weyhermuller T, Wieghardt K. Dalton Trans. 2003:1126–1132.

38. Carter SM, Sia A, Shaw MJ, Heyduk AF. J. Am. Chem. Soc. 2008;130:5838.

39. Johnson MK. In: Physical Methods in Bioinorganic Chemistry. Lawrence Que J, editor. University Science Books; Sausalito, CA: 2000. pp. 233–286.

40. **a.** Neese F, Solomon EI. Inorg. Chem. 1998;37:6568–6582.
b. Neese F, Solomon EI. Inorg. Chem. 1999;38:1847–1865.

41. **a.** Pavel EG, Kitajima N, Solomon EI. J. Am. Chem. Soc. 1998;120:3949–3962.
b. Solomon EI. Inorg. Chem. 2001;40:3656–3669.

42. **a.** Verma P, Weir J, Mirica L, Stack TDP. Inorg. Chem. 2011;50:9816–9825.
b. Dunn TJ, Ramogida CF, Simmonds C, Paterson A, Wong EWY,

Chiang L, Shimazaki Y, Storr T. Inorg. Chem. 2011;50:6746–6755.
c. Holt BTO, Vance MA, Mirica LM, Heppner DE, Stack TDP, Solomon EI. J. Am. Chem. Soc. 2009;131:6421–6438.
d. Hartl F, Stufkens DJ, Vlcek A. Inorg. Chem. 1992;31:1687–1695.

43. Vlcek A. Comments Inorg. Chem. 1994;16:207–228.

44. To the best of our knowledge, Wieghardt and coworkers have not explored the reduction of their five-coordinate $[Fe^{3+}(ISQ)_2X]$ complexes (X = Cl, Br, I, N_3). However, the square-pyramidal, trianionic coordination environment likely lowers the potential of the Fe(III) center, favoring ligand-based reduction.

45. Ogihara T, Hikichi S, Akita M, Moro-oka Y. Inorg. Chem. 1998;37:2614–2615.

46. Kitajima N, Fujisawa L, Fujimoto C, Moro-oka Y, Hashimoto S, Kitagawa T, Toriumi K, Tatsumi K, Nakamura A. J. Am. Chem. Soc. 1992;114:1277–1291.

47. Khomenko TM, Salomatina OV, Kurbakova SY, Il'ina IV, Volcho KP, Komarova NI, Korchagina DV, Salakhutdinov NF, Tolstikov AG. Russ. J. Org. Chem. 2006;42:1653–1661.

48. Manner VW, Markle TF, Freudenthal JH, Roth JP, Mayer JM. Chem. Commun. 2008:256–258.

49. Cherkasov V, Druzhkov N, Kocherova T, Fukin G, Shavyrin A. Tetrahedron. 2011;67:80–84.

50. Sheldrick GM. Acta Crystallogr. Sect. A. 2008;64:112–122.

51. Dolomanov OV, Bourhis LJ, Gildea RJ, Howard JAK, Puschmann H. J. Appl. Crystallogr. 2009;42:339–341.

52. Neese F. ORCA - An ab initio, Density Functional and Semi-empirical Program Package, version 2.8. University of Bonn; Bonn, Germany: 2010.

53. **a.** Becke AD. J. Chem. Phys. 1986;84:4524–4529.
b. Perdew JP. Physical Review B. 1986;33:8822–8824.

54. **a.** Becke AD. J. Chem. Phys. 1993;98:5648–5652.
b. Lee CT, Yang WT, Parr RG. Physical Review B. 1988;37:785–789.

Chemistry, a European Journal, Vol. 19, No. 29 (July 2013): pg. 9686-9698. DOI.

55. **a.** Schafer A, Horn H, Ahlrichs R. J. Chem. Phys. 1992;97:2571–2577.
b. Schafer A, Huber C, Ahlrichs R. J. Chem. Phys. 1994;100:5829–5835.

56. **a.** Stratmann RE, Scuseria GE, Frisch MJ. J. Chem. Phys. 1998;109:8218–8224.
b. Casida ME, Jamorski C, Casida KC, Salahub DR. J. Chem. Phys. 1998;108:4439–4449.
c. Bauernschmitt R, Ahlrichs R. Chem. Phys. Lett. 1996;256:454–464.

57. **a.** Hirata S, Head-Gordon M. Chem. Phys. Lett. 1999;314:291–299.
b. Hirata S, Head-Gordon M. Chem. Phys. Lett. 1999;302:375–382.

58. Romelt M, Ye SF, Neese F. Inorg. Chem. 2009;48:784–785. [PubMed]

59. Laaksonen L. J. Mol. Graph. 1992;10:33. [PubMed]

About the Authors

Dr. Codrina V. Popescu : Department of Chemistry, Ursinus College, Collegeville, Pennsylvania 19426 (USA).

Fax: (+1) 414-288-7066

Email: cpopescu@ursinus.edu

Dr. Adam T. Fiedler : Department of Chemistry, Marquette University, Milwaukee, Wisconsin 53201 (USA).

Fax: (+1) 414-288-7066

Email: adam.fiedler@marquette.edu

Chemistry, a European Journal, Vol. 19, No. 29 (July 2013): pg. 9686-9698. DOI.